Spatially Resolved Stellar Kinematics from LEGA-C: Increased Rotational Support in $z \sim 0.8$ Quiescent Galaxies

Rachel Bezanson[1,2], Arjen van der Wel[3,4] , Camilla Pacifici[5] , Kai Noeske[4], Ivana Barišić[4] , Eric F. Bell[6] ,
Gabriel B. Brammer[5] , Joao Calhau[7], Priscilla Chauke[4] , Pieter van Dokkum[8] , Marijn Franx[9] , Anna Gallazzi[10] ,
Josha van Houdt[4], Ivo Labbé[9] , Michael V. Maseda[9] , Juan Carlos Muños-Mateos[11], Adam Muzzin[12] , Jesse van de Sande[13] ,
David Sobral[7,9], Caroline Straatman[3] , and Po-Feng Wu[4]

[1] Department of Physics and Astronomy and PITT PACC, University of Pittsburgh, Pittsburgh, PA 15260, USA; rachel.bezanson@pitt.edu
[2] Department of Astrophysics, Princeton University, Princeton, NJ 08544, USA
[3] Sterrenkundig Observatorium, Universiteit Gent, Krijgslaan 281 S9, B-9000 Gent, Belgium
[4] Max-Planck Institut für Astronomie, Königstuhl 17, D-69117, Heidelberg, Germany
[5] Space Telescope Science Institute, 3700 San Martin Drive, Baltimore, MD 21218, USA
[6] Department of Astronomy, University of Michigan, 1085 South University Avenue, Ann Arbor, MI 48109, USA
[7] Department of Physics, Lancaster University, Lancaster LA1 4 YB, UK
[8] Astronomy Department, Yale University, New Haven, CT 06511, USA
[9] Leiden Observatory, Leiden University, P.O. Box 9513, NL-2300 AA Leiden, The Netherlands
[10] INAF-Osservatorio Astrofisico di Arcetri, Largo Enrico Fermi 5, I-50125 Firenze, Italy
[11] European Southern Observatory, Alonso de Crdova 3107, Casilla 19001, Vitacura, Santiago, Chile
[12] Department of Physics and Astronomy, York University, 4700 Keele St., Toronto, Ontario, MJ3 1P3, Canada
[13] Sydney Institute for Astronomy, School of Physics, A28, The University of Sydney, NSW, 2006, Australia
Received 2017 June 26; revised 2018 April 5; accepted 2018 April 5; published 2018 May 4

Abstract

We present stellar rotation curves and velocity dispersion profiles for 104 quiescent galaxies at $z = 0.6$–1 from the Large Early Galaxy Astrophysics Census (LEGA-C) spectroscopic survey. Rotation is typically probed across 10–20 kpc, or to an average of $2.7R_e$. Combined with central stellar velocity dispersions (σ_0) this provides the first determination of the dynamical state of a sample selected by a lack of star formation activity at large lookback time. The most massive galaxies ($M_\star > 2 \times 10^{11} M_\odot$) generally show no or little rotation measured at 5 kpc ($|V_5|/\sigma_0 < 0.2$ in eight of ten cases), while $\sim 64\%$ of less massive galaxies show significant rotation. This is reminiscent of local fast- and slow-rotating ellipticals and implies that low- and high-redshift quiescent galaxies have qualitatively similar dynamical structures. We compare $|V_5|/\sigma_0$ distributions at $z \sim 0.8$ and the present day by re-binning and smoothing the kinematic maps of 91 low-redshift quiescent galaxies from the Calar Alto Legacy Integral Field Area (CALIFA) survey and find evidence for a decrease in rotational support since $z \sim 1$. This result is especially strong when galaxies are compared at fixed velocity dispersion; if velocity dispersion does not evolve for individual galaxies then the rotational velocity at 5 kpc was an average of $94 \pm 22\%$ higher in $z \sim 0.8$ quiescent galaxies than today. Considering that the number of quiescent galaxies grows with time and that new additions to the population descend from rotationally supported star-forming galaxies, our results imply that quiescent galaxies must lose angular momentum between $z \sim 1$ and the present, presumably through dissipationless merging, and/or that the mechanism that transforms star-forming galaxies also reduces their rotational support.

Key words: galaxies: elliptical and lenticular, cD – galaxies: evolution – galaxies: high-redshift –
galaxies: kinematics and dynamics – galaxies: structure

Supporting material: machine-readable table

1. Introduction

Massive galaxies exhibit significant angular momentum at $z \sim 2$ (e.g., Förster Schreiber et al. 2009, 2011; Tacconi et al. 2013; van der Wel et al. 2014a; van Dokkum et al. 2015; Wisnioski et al. 2015; Belli et al. 2017; Straatman et al. 2017). This statement is in contrast with massive galaxies in the local universe, which are predominantly elliptical, where even so-called "fast-rotators" exhibit significant dispersion support (e.g., Emsellem et al. 2007, 2011). This discrepancy necessitates an evolution in rotational support through cosmic time; however, how and why this change occurred remains up for debate. One possibility is that the quenching process itself destroys organized rotation and/or the destruction of organized rotation is effectively what quenches galaxies (e.g., Hopkins et al. 2008; Martig et al. 2009). Alternatively the evolution could be more gradual, owing to subsequent minor or major merging (e.g., Naab et al. 2009, 2014; Hilz et al. 2013). We have

evidence that the latter must play some role from the size evolution of quiescent, or "non-star-forming," galaxies, which grow significantly in size on average through cosmic time (e.g., Daddi et al. 2005; Toft et al. 2007; Trujillo et al. 2007; van der Wel et al. 2008, 2014b; van Dokkum et al. 2008; Newman et al. 2012 and references therein). This growth is most likely due to dissipationless minor merging (e.g., Bezanson et al. 2009; Hopkins et al. 2009; Naab et al. 2009; van Dokkum et al. 2010; Oser et al. 2011) which would diminish net angular momentum. For a given population of quiescent galaxies the rate of stellar rotation should then decrease with cosmic time, implying that high-redshift quiescent galaxies would show more rotation than their present-day counterparts.

A complicating factor is that the high- and low-redshift populations cannot be directly compared due to the increase in the number of quiescent galaxies with cosmic time, as galaxies cease to form stars, or "quench." This effect, often called

progenitor bias, has been investigated thoroughly as a potential driver of the empirical size evolution of quiescent galaxies as new and more extended additions to the red sequence would drive evolution in the average size–mass relations (e.g., van der Wel et al. 2009; Valentinuzzi et al. 2010a, 2010b; Carollo et al. 2013; Poggianti et al. 2013; Fagioli et al. 2016; Lilly & Carollo 2016; Williams et al. 2016). Although there is evidence for some evolution in the velocity dispersions of star-forming galaxies through cosmic time, these galaxies have been shown to be primarily rotating disks since at least $z \sim 2$ (e.g., Wisnioski et al. 2015; Simons et al. 2017). Without any structural transformation, these new additions would also represent an influx of still-rotating quiescent galaxies as they have had less time since quenching to lose their angular momentum than their older counterparts. Therefore, the fraction of rotating galaxies in the quiescent population may increase over cosmic time. One further level of complexity in this picture is that quenching of star formation may coincide with a change in dynamical structure, as suggested by the smaller relative sizes of post-starburst galaxies that constitute the newest additions to the high-redshift quiescent population (Whitaker et al. 2012a; Yano et al. 2016).

So far, evolution in the shape distribution of quiescent galaxies has provided one of the strongest constraints on the evolution of angular momentum among the population of quiescent galaxies. The emerging picture is that oblate, flat shapes are more common among high-redshift quiescent galaxies than in the present-day universe (van der Wel et al. 2011; Chevance et al. 2012; Chang et al. 2013). The (projected) shape of a galaxy is obviously only a crude proxy of dynamical structure, and even for large samples the necessary assumption was made that the population of high-redshift quiescent galaxies was composed of galaxies with the same intrinsic shapes as today's galaxies: oblate disks and triaxial spheroids. The relative numbers of both types were then inferred to change with redshift (Chang et al. 2013).

However, it is not self-evident that galaxy structures are the same at different cosmic epochs and the correspondence between global shape and kinematic properties may well evolve. Therefore, it is essential to obtain spatially resolved kinematics of high-redshift quiescent galaxies, which must be measured from stellar absorption features. Currently, such direct evidence comes from small samples without uniform or necessarily representative selections. These include two examples of strongly lensed galaxies at $z \sim 2$ (Newman et al. 2015; Toft et al. 2017) and samples of 25 $z \sim 0.5$ cluster (Moran et al. 2007; van der Marel & van Dokkum 2007) and $z \sim 1$ field galaxies (van der Wel & van der Marel 2008). The latter samples were selected on the basis of visual morphology, that is, a visual determination of the absence of a disk-like structure, preventing a rigorous analysis of the evolution of rotation among quiescent galaxies at different epochs. Finally, Belli et al. (2017) found indirect evidence of evolution in the rotational support of quiescent galaxies from dynamical masses. In this paper we present a much larger sample of $\sim$100 galaxies at $z \sim 0.8$ selected by their lack of star formation activity and with high-quality stellar rotation curves from the Large Early Galaxy Astrophysics Census (LEGA-C) survey.

This paper begins in Section 2 with a brief description of the LEGA-C survey and the extraction of spatially resolved stellar kinematics. In Section 3 we investigate the empirically derived rotational support of massive quiescent galaxies at $z \sim 0.8$ and the trends of that rotation with galaxy properties derived from imaging data. In Section 4 we use stellar kinematics derived from the Calar Alto Legacy Integral Field Area (CALIFA) DR3 data set to assess the effects of seeing on the LEGA-C observations and study the redshift-evolution of the rotational support of massive quiescent galaxies. Finally in Section 5, we conclude with a discussion of these results in the context of models of galaxy evolution and other observational and theoretical studies. Throughout this paper we assume a standard concordance cosmology ($H_0 = 70 \text{ km s}^{-1} \text{ Mpc}^{-1}$, $\Omega_M = 0.3$, and $\Omega_\Lambda = 0.7$).

2. LEGA-C Data and Stellar Kinematics

2.1. The LEGA-C Spectroscopic Survey

The spectroscopic data included in this analysis are drawn from the first year data release of the LEGA-C survey (van der Wel et al. 2016). This project is a 128 night ESO Public Spectroscopic survey of massive galaxies at $0.6 < z < 1.0$ in the COSMOS field using VIMOS on the VLT. The LEGA-C survey primary sample of $\sim$3000 galaxies is selected with a photometric or spectroscopic redshift-dependent K-magnitude limit ($K = 20.7 - 7.5 \times \log((1 + z)/1.8)$), corresponding to a representative sampling of galaxy colors down to $\log M_\star/M_\odot \gtrsim 10.4$. The defining, unique aspect of the LEGA-C spectra is the deep 20 hr long integration at a resolution of $R = 2500$ in the wavelength range $\sim$6300–8800 Å. The first year data set consists of seven masks of roughly 130 galaxies in each mask with slits that are oriented in the N–S direction. The combined data yield the extremely high signal-to-noise ratio $S/N \sim 20 \text{ Å}^{-1}$ in the continuum. The data reduction procedure is described by van der Wel et al. (2016). Two-dimensional and extracted 1D reduced spectra are publicly available via the ESO Science Archive Facility.

2.2. Photometry: Stellar Populations and Structures

Additional ancillary data are available for the LEGA-C sample in the COSMOS field. Targeted galaxies are selected from the UltraVISTA version DR1 4.1 K-selected catalogs (Muzzin et al. 2013a). Rest-frame colors are calculated from the UltraVISTA photometry (McCracken et al. 2012; Muzzin et al. 2013a) using the EAZY (Brammer et al. 2008) code and fixing redshifts to the LEGA-C spectroscopic redshifts. Stellar population properties, most notably stellar masses, are determined from the UltraVISTA photometry using the FAST code (Kriek et al. 2009) and using Bruzual & Charlot (2003) stellar population libraries, adopting a Chabrier (2003) Initial Mass Function (IMF), Calzetti et al. (2000) dust extinction, and exponentially declining star formation rates (SFRs). Although formal uncertainties on stellar masses are relatively low, systematics likely dominate and we adopt an uncertainty of 0.2 dex following Muzzin et al. (2009). SFRs are estimated from the UV and IR (24 μm from *Spitzer*–MIPS) luminosities, following Whitaker et al. (2012b). Morphological information is derived for all galaxies from COSMOS *Hubble Space Telescope* (*HST*) ACS F814W imaging (Koekemoer et al. 2007; Massey et al. 2010), which is well matched to the rest-frame optical at this redshift. Best-fit Sérsic parameters, and uncertainties are derived for all LEGA-C galaxies using

GALFIT (Peng et al. 2002) and GALAPAGOS (Barden et al. 2012) following the procedures outlined in van der Wel et al. (2012, 2016). The quoted measurement uncertainties of structural parameters do not include a number of systematic uncertainties and specifically do not account for covariance of parameters, which could dominate ,e.g., for Sérsic parameters. For visual presentation, we match the LEGA-C catalog to imaging from the first public data release of the Hyper-Suprime Cam Subaru Strategic Program (HSC-SSP), which includes deep *grizy* imaging in the COSMOS field (Aihara et al. 2018).

Stellar population and structural properties for the year one LEGA-C massive galaxies are shown in Figure 1. Symbol color indicates whether galaxies are categorized as quiescent (red) or star-forming (blue) based on their rest-frame $U - V$ and $V - J$ colors (upper left panel), adopting the Muzzin et al. (2013b) color cuts, which are specifically defined for the UltraVISTA photometric catalogs used in determining rest-frame colors. We note that, although this selection does a very good job of identifying galaxies with quiescent stellar populations, there is a subset of galaxies in the current sample with clearly detected emission lines (see Figure 2 for examples). The properties of galaxies in this sample (redshift, stellar mass, Sérsic profile parameters, velocities and σ_0) are included in Table 1.

Horizontal lines indicate galaxies included in the full sample for which the semimajor axis is significantly inclined with respect to the VIMOS slits ($|PA| \geqslant 45°$). These objects are not considered in this paper, as the mismatch between the kinematic axis and the slit will prevent us from tracing stellar rotation in a straightforward manner (e.g., Weiner et al. 2006; Straatman et al. 2017). For this paper we focus on major axis kinematics in the 104 quiescent galaxies for which the major axes are aligned to within $|PA| < 45°$ of the N–S slits (circles in Figure 1). We note that the quoted position angles are photometric and the kinematic axes can also be misaligned with the photometry (e.g., Franx et al. 1989; Emsellem et al. 2007). Emsellem et al. (2007) demonstrated that for fast rotators this effect is minimal ($\lesssim 10\%$), but kinematic and photometric position angles can be significantly misaligned, by up to $\sim 50\%$ in the SAURON sample. However Krajnović et al. (2011) showed that for 90% of galaxies in the ATLAS3D sample, the kinematic misalignment will be $\leqslant 15°$.

The top right panel of Figure 1 shows the rest-frame $U - V$ colors of the two populations as a function of stellar mass. The bottom left panel shows the effective radius along the semimajor axis versus stellar mass, with the solid, red diagonal line indicating the van der Wel et al. (2014b) size–mass relation for quiescent galaxies and the dashed blue line for star-forming galaxies. Finally, the bottom right panel shows the specific star formation rate (sSFR) versus stellar mass. We note here that SFRs determined for quiescent galaxies are notably uncertain and, as 24 micron flux may be undetected or ambiguous, these sSFRs are likely to be upper limits for our sample of galaxies. The quiescent and star-forming galaxies in the LEGA-C sample exhibit different distributions in all four phase spaces, although the populations overlap slightly in all but the $U - V$ and $V - J$ colors, which are used to initially differentiate between them.

2.3. Spatially Resolved Stellar Kinematics

We measure the stellar and gas phase line-of-sight kinematics for each galaxy using the penalized pixel-fitting (pPXF) method (Cappellari & Emsellem 2004) with the updated Python routines (Cappellari 2017). For each 2D LEGA-C spectrum, each row with median $S/N > 2$ per pixel is fit with two template sets that are allowed to independently shift and broaden: stellar population templates to fit the continuum and a collection of possible emission lines to fit the ionized gas emission. The stellar template is a linear, optimal non-negative combination of Vazdekis (1999) single stellar population models, which are based on the Medium-resolution INT Library of Empirical Spectra (MILES) (Sánchez-Blázquez et al. 2006) empirical stellar spectra combined using Girardi et al. (2000) isochrones. We extend the rotation curve measurements in the outer rows (with $S/N < 2$) by fixing the velocity dispersion to $\sigma = 150 \text{ km s}^{-1}$ and allowing the normalization and velocity offsets to vary for both stellar and gas templates and find stable results to $S/N \gtrsim 1.2$ per pixel. This yields line-of-sight velocity measures out to an average of 8.8 kpc or $2.7 R_e$. We verify that fixing the velocity dispersion to the nearest measured value does not significantly alter the measured rotational velocities, on average leading to a 2% ($\Delta V = 1.2 \text{ km s}^{-1}$) offset, which is well within the measurement uncertainty.

Emission line templates are treated as a single kinematic component, but the normalization of each line (Balmer lines: H10, H9, H8, Hϵ, Hδ, Hγ, Hβ, Hα; [Ne V], [Ne VI], [Ne III], and [O II] and [O III] doublets) is a free parameter in the fit. The optimally extracted 1D spectra and best-fit models are shown in Figure 2 for three galaxies with increasing emission line components. These galaxies are representative (e.g., in S/N), but are selected to demonstrate the necessity of including emission lines in the kinematic fits and the ability of the data to identify emission lines as they fill in broader absorption features. The majority of galaxies in the sample do not have detected emission lines. Images of each galaxy are shown on the left from the COSMOS *HST* v2.0 ACS Mosaics (top) (Koekemoer et al. 2007) and *gri* composite color images from the HSC-SSP (Aihara et al. 2018). The 2D spectrum is included in the top panel for each galaxy, with the best-fit rotation curve derived from stellar kinematics at the position of a number of strong absorption (red lines) and emission (blue lines) features overplotted. The middle panel shows the 1D optimally extracted spectrum for each galaxy with the best-fitting continuum model in red and for the second and third galaxies the emission line and total models in blue and purple. The bottom panel in each row shows the residuals from the fit, which are minimal and in most cases uncorrelated.

These fits yield spatially resolved line-of-sight stellar and gas velocity and velocity dispersion profiles along the N–S slits. Although emission lines are present due to residual ionized gas (primarily the [O II] doublet) in a subset of this quiescent galaxy sample, we focus our analysis on the kinematics derived from fitting the stellar continuum of each galaxy. Measured stellar rotation curves are shown in Figure 3, in which velocity of the stellar component is indicated by black points and stellar velocity dispersion profiles are shown in red. Rotation curves are plotted in order of increasing rotational velocity, separated by page in decreasing mass bins. We fit the rotation curves with an arctangent model and define the line-of-sight rotational velocity (V_5) of a galaxy as the value of the best-fitting arctangent at a radius of 5 kpc along the slit. This distance is not corrected for inclination or slit misalignment. We define the central velocity dispersion (σ_0) as the velocity dispersion

Table 1
Properties of Quiescent Galaxies in the LEGA-C Sample

ID	z_{spec}	$\log(\frac{M_\star}{M_\odot})$	R_e (arcsec)	b/a	PA (degrees)	n	V_5 (km s^{-1})	V_{Re} (km s^{-1})	V_{max} (km s^{-1})	σ_0 (km s^{-1})
(1)	(2)	(3)	(4)	(5)	(6)	(7)	(8)	(9)	(10)	(11)
80755	0.7325	10.9	1.05 ± 0.02	0.51 ± 0.00	27.54 ± 0.45	3.90 ± 0.08	−68.6 ± 4.6	−61.9 ± 4.4	−116.4 ± 9.7	197.0 ± 8.4
87345	0.6226	10.7	0.67 ± 0.00	0.54 ± 0.00	−35.46 ± 0.26	3.13 ± 0.04	89.7 ± 2.1	51.9 ± 2.2	138.7 ± 2.1	157.5 ± 5.2
88863	0.8124	10.4	0.20 ± 0.00	0.91 ± 0.01	−32.43 ± 0.61	2.62 ± 0.06	−99.0 ± −99.0	−99.0 ± −99.0	−99.0 ± −99.0	96.8 ± 7.1
90664	0.7480	10.2	0.07 ± 0.00	0.50 ± 0.01	−5.14 ± 1.50	4.66 ± 0.17	−13.2 ± 11.8	−3.6 ± 6.2	−12.9 ± 6.3	140.1 ± 17.8
94494	0.7401	10.9	0.49 ± 0.00	0.95 ± 0.00	39.50 ± 0.30	3.72 ± 0.05	92.0 ± 1.0	63.1 ± 0.7	165.3 ± 1.4	215.5 ± 3.9
97994	0.9821	11.2	0.57 ± 0.01	0.64 ± 0.01	19.79 ± 0.48	2.61 ± 0.06	115.8 ± 6.1	83.6 ± 4.4	189.3 ± 8.9	236.6 ± 17.6
105208	0.9345	10.8	0.64 ± 0.02	0.85 ± 0.01	31.85 ± 0.68	5.74 ± 0.20	−31.1 ± 10.5	−27.4 ± 9.3	−55.3 ± 20.7	203.0 ± 22.9
107468	0.9178	11.1	0.21 ± 0.00	0.24 ± 0.00	24.21 ± 0.35	2.27 ± 0.03	−97.8 ± 3.0	−15.1 ± 1.1	−122.4 ± 1.9	234.0 ± 6.2
107489	0.8383	11.1	0.32 ± 0.00	0.44 ± 0.00	26.75 ± 0.26	2.29 ± 0.03	29.8 ± 4.0	7.6 ± 1.0	60.5 ± 2.0	383.6 ± 7.0
108227	0.9603	11.4	1.66 ± 0.03	0.55 ± 0.01	−31.66 ± 0.54	1.30 ± 0.03	−28.0 ± 5.7	−43.5 ± 9.8	−59.2 ± 24.0	263.9 ± 17.0
108472	0.6671	10.6	0.14 ± 0.00	0.56 ± 0.01	8.52 ± 0.68	3.72 ± 0.07	−69.5 ± 2.1	−12.2 ± 0.4	−139.8 ± 0.8	160.8 ± 4.2
110509	0.6671	11.0	0.99 ± 0.01	0.95 ± 0.00	33.81 ± 0.23	3.76 ± 0.04	23.9 ± 1.5	29.6 ± 2.0	41.6 ± 5.8	217.4 ± 5.0
110805	0.7292	10.6	0.47 ± 0.00	0.21 ± 0.00	12.40 ± 0.22	0.55 ± 0.01	−151.5 ± 3.0	−70.4 ± 2.7	−178.8 ± 2.3	172.7 ± 7.5
111188	0.9164	10.9	0.43 ± 0.01	0.58 ± 0.01	11.23 ± 0.65	5.62 ± 0.19	−53.3 ± 9.5	−46.3 ± 5.7	−55.7 ± 13.5	180.1 ± 10.1
112200	0.8279	10.6	0.29 ± 0.01	0.86 ± 0.01	36.97 ± 0.77	4.21 ± 0.15	3.5 ± 8.5	1.3 ± 5.1	3.2 ± 7.1	151.6 ± 13.7
112534	0.9837	11.0	0.34 ± 0.01	0.50 ± 0.01	−21.17 ± 0.60	1.89 ± 0.06	−107.5 ± 7.8	−45.0 ± 5.5	−159.7 ± 7.3	297.3 ± 19.9
116829	0.6683	10.8	0.45 ± 0.00	0.70 ± 0.00	22.15 ± 0.29	2.46 ± 0.03	−1.5 ± 2.0	−1.5 ± 1.7	−1.5 ± 2.0	162.3 ± 6.7
117010	0.6766	10.4	0.40 ± 0.01	0.54 ± 0.01	−27.19 ± 0.61	4.45 ± 0.13	99.0 ± 3.4	36.3 ± 1.8	135.3 ± 2.7	158.1 ± 5.3
117400	0.6687	11.3	0.80 ± 0.01	0.79 ± 0.00	40.78 ± 0.28	4.85 ± 0.06	1.3 ± 3.7	1.2 ± 3.5	3.1 ± 5.3	258.2 ± 4.7
117692	0.6753	10.8	0.63 ± 0.01	0.48 ± 0.00	−22.70 ± 0.34	4.13 ± 0.07	−100.9 ± 2.4	−54.2 ± 1.4	−189.4 ± 2.6	185.4 ± 7.3

Note. This table includes measured properties of the galaxies included in this sample from the year one LEGA-C data set. All galaxies included in this table are well-aligned with the N–S VIMOS slits (|PA| < 45°), quiescent based on Muzzin et al. (2013b) $U − V$ and $V − J$ rest-frame color cuts, have reliable morphological parameters measured from ACS F814 images, and represent single virialized systems. Columns: (1) ID from the Muzzin et al. (2013a) UltraVISTA DR1 v4.1 catalogs; (2) spectroscopic redshift; (3) log stellar mass assuming a Chabrier (2003) IMF; (4) Sérsic semimajor axis; (5) projected axis ratio; (6) major axis position angle; (7) Sérsic index; (8) average line-of sight rotational velocity measured at 5 kpc; (9) average line-of sight rotational velocity measured at the effective radius; (10) average line-of sight rotational velocity measured at the maximum extent; (11) velocity dispersion measured in the central pixel in the spatial dimension.

(This table is available in its entirety in machine-readable form.)
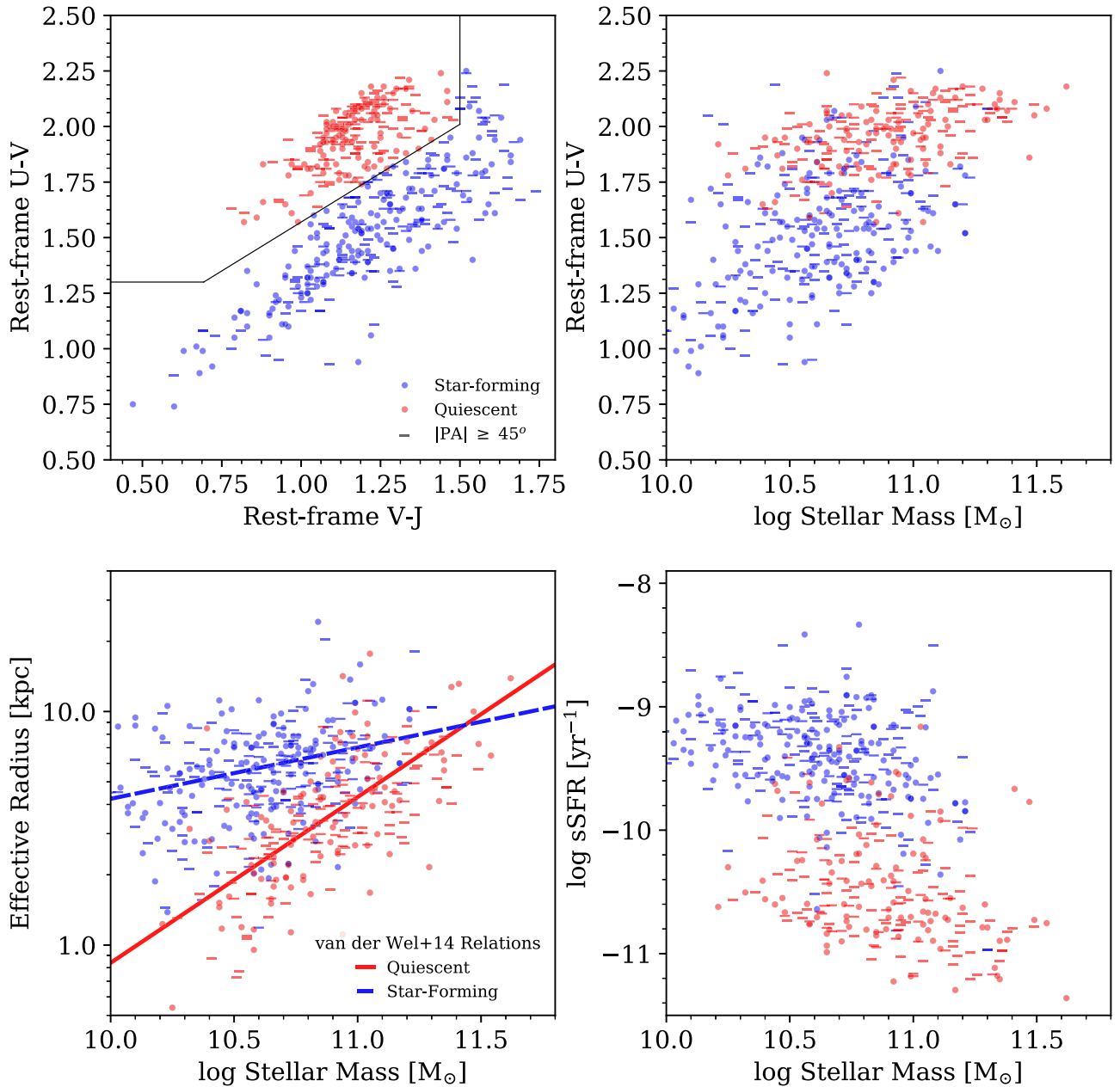
Figure 1. Properties of the complete LEGA-C year one data set. Symbol colors differentiate between star-forming (blue) and quiescent (red) galaxies as determined by $U - V$ and $V - J$ rest-frame colors and cuts from Muzzin et al. (2013b) (upper left panel). Misaligned galaxies ($|PA| \geqslant 45°$) are excluded from this study and are indicated by horizontal lines. Star-forming and quiescent galaxies in the LEGA-C sample have different distributions in color (upper right panel), physical size (bottom left panel), and specific star formation rate (bottom right panel); for this study we focus on the kinematics of the quiescent population.

measured in the central pixel ($0\rlap{.}''205$), which is set as the brightest pixel in the spatial profile. Uncertainties in V_5 are estimated by bootstrap resampling within the velocity errors and errors in velocity dispersion are formal uncertainties estimated by pPXF, with a small correction to underestimated formal errors based on the measured relationship between the measured S/N and formal errors.

We adopt this definition of rotational velocity within a fixed physical aperture for two primary reasons. First, the effects of seeing will be similar within a fixed physical radius as opposed to an aperture that scales with the galaxy size. The 5 kpc aperture is used because it is the approximate extent of the shortest LEGA-C rotation curves, and therefore requires minimal extrapolation. Second, utilizing a fixed aperture allows

for comparison with galaxies at low redshift in Section 4 within the same physical region of the galaxy and will be less sensitive to differing apertures due to real size evolution in the galaxy populations. We discuss the impact of this choice of aperture, including the effects of adopting an evolving aperture or utilizing the maximum observed velocity, in Appendix B.

Given that the effective seeing, including atmospheric and alignment effects, is comparable to the spatial extent of the galaxies themselves (FWHM $\sim 1\rlap{.}''0 \approx 7\,$kpc) the effects of beam smearing will be significant and kinematic measurements at each pixel ($0\rlap{.}''205$) are not independent. This results in shallower than intrinsic rotation curves and elevated line-of-sight velocity dispersions. Dynamical modeling that accounts for aperture and beam smearing effects, which is common in
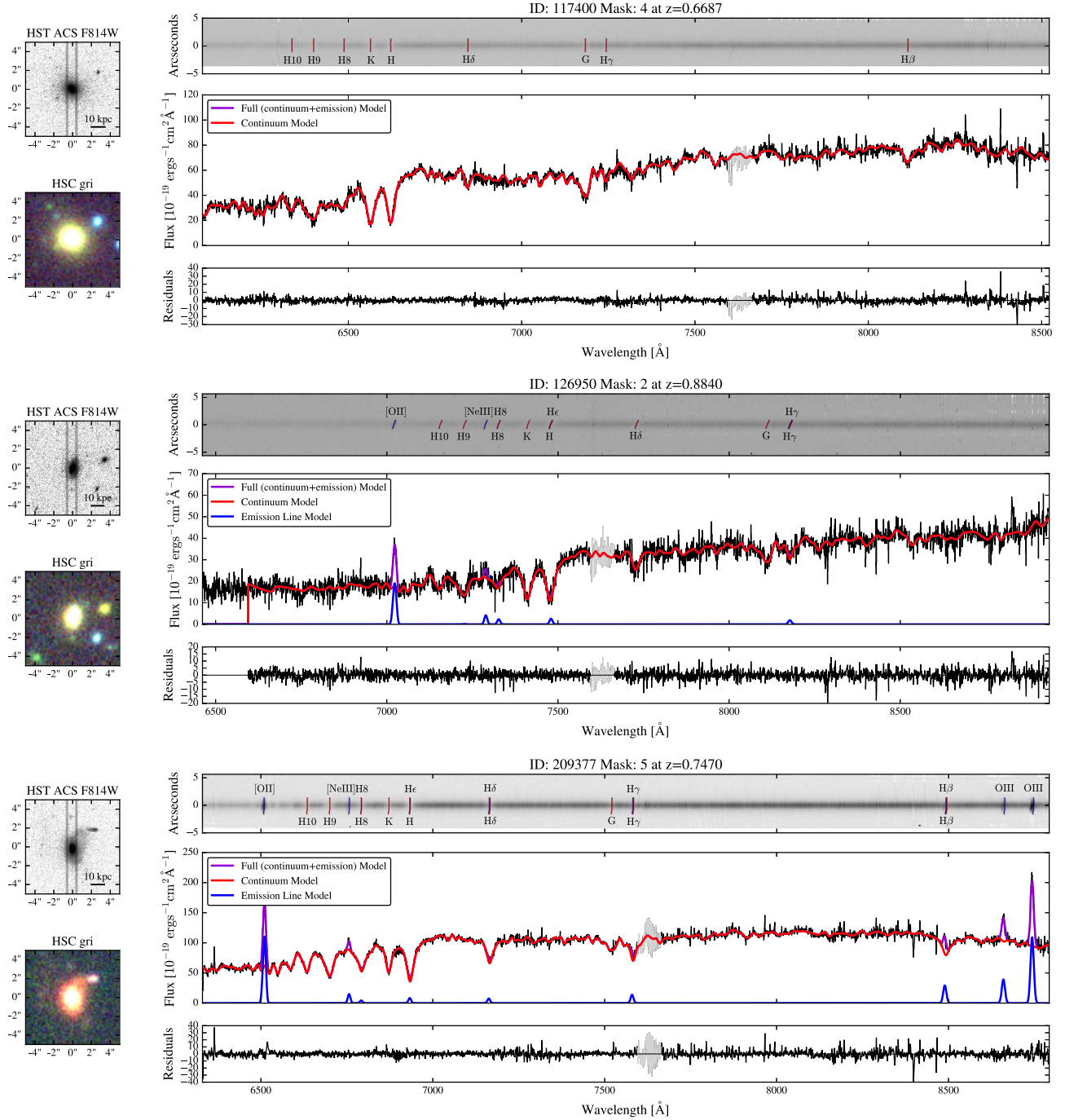
Figure 2. Images and spectra of three example quiescent galaxies from the LEGA-C sample, selected to span a range in emission line flux for demonstration of fitting; most galaxies in the sample do not exhibit significant emission. Images from *HST* ACS COSMOS mosaics and gri color images from the HSC-SSP public data release. The position and width of the LEGA-C slit as well as the physical scale are indicated on the *HST* image. The top panel in each row shows the 2D LEGA-C spectrum, with the location of spectral absorption and emission features, including the measured rotation, indicated with blue and red lines. Emission line features are labeled above the galaxy spectrum and continuum features are indicated below. One-dimensional optimally extracted spectra are included in the middle panel to demonstrate the continuum plus emission-line modeling. Best-fit continuum models are indicated by red lines, emission lines, where detected, are indicated by blue lines, and the combined model by purple lines. Residuals from the 1D fit are included in the bottom panel. In this work, this procedure is repeated separately on all rows with sufficient S/N in the 2D spectra.

the analysis of emission line kinematics at high redshift (e.g., Vogt et al. 1996, 1997; Weiner et al. 2006; Kassin et al. 2007; Simons et al. 2015, 2016; Price et al. 2016; Wuyts et al. 2016; Harrison et al. 2017; Straatman et al. 2017) can reconstruct the intrinsic rotation and velocity dispersion profiles, given modeling assumptions, for direct comparisons with present-day galaxy samples. Such modeling efforts are underway (J. van Houdt et al. 2018, in preparation), but beyond the scope of the current paper; here we focus on the directly measured rotation (V_5) and rotational support ($|V_5|/\sigma_0$). In Section 4 we reconstruct the rotation and dispersion profiles of local galaxies as they would be observed with LEGA-C at $z \sim 0.8$.
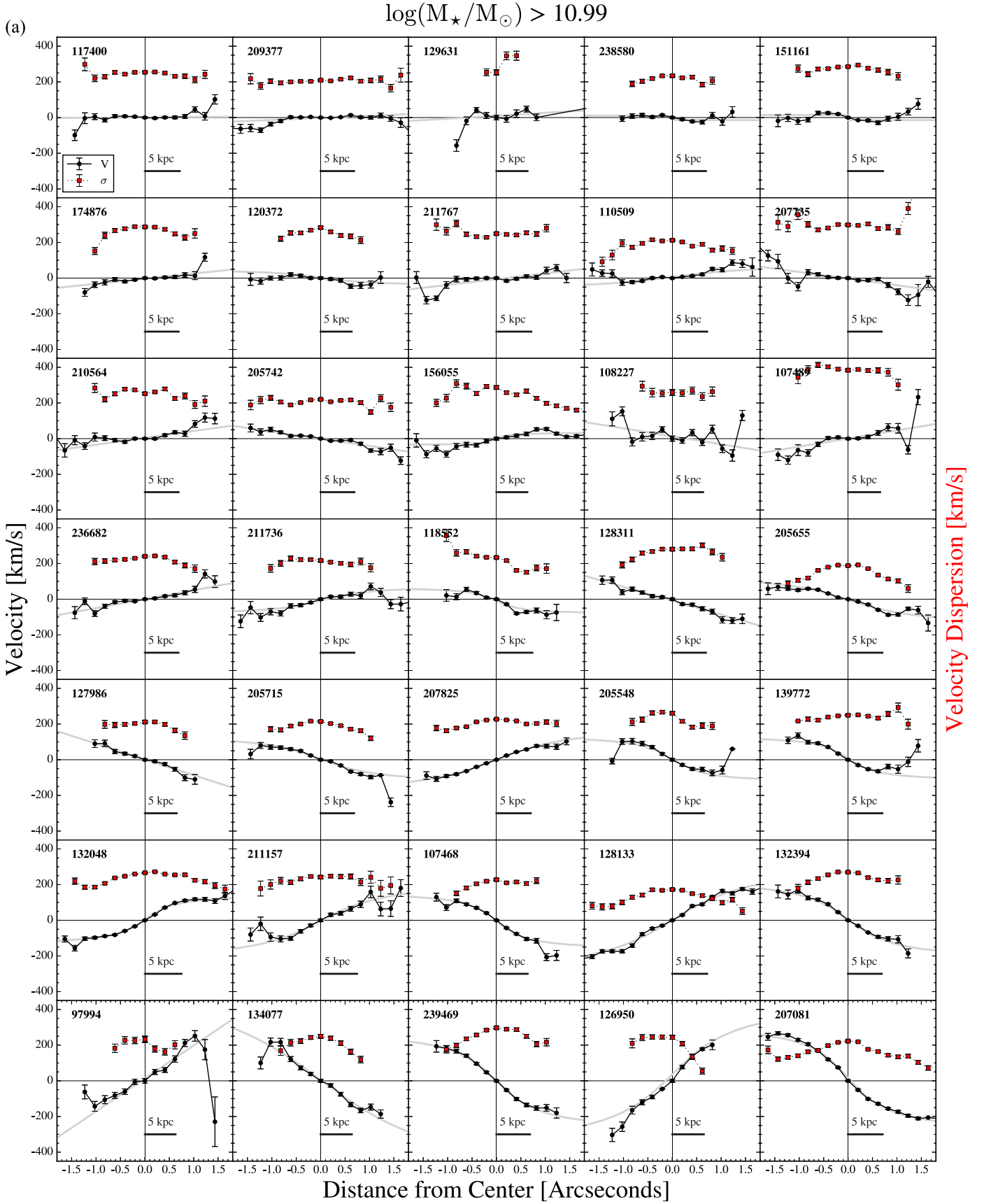
Figure 3. (a) Stellar rotation curves (black) and velocity dispersion profiles (red) for the 35 highest-mass ($\log M_*/M_\odot > 11$) quiescent galaxies, ordered by increasing V_5. The rotational velocity is defined as the velocity of the best-fitting arctangent function (indicated by the gray solid lines) at a radius of 5 kpc (indicated by the black bars) from the central pixel. (b) Stellar rotation curves (black) and velocity dispersion profiles (red) for the 35 intermediate-mass ($10.7 < \log M_*/M_\odot \leqslant 11$) quiescent galaxies. (c) Stellar rotation curves (black) and velocity dispersion profiles (red) for the lowest-mass ($\log M_*/M_\odot < 10.7$) sample of quiescent galaxies in LEGA-C.

$$10.73 < \log(M_{\star}/M_{\odot}) \leq 10.99$$

Figure 3. (Continued.)

$$\log(M_\star/M_\odot) \leq 10.73$$
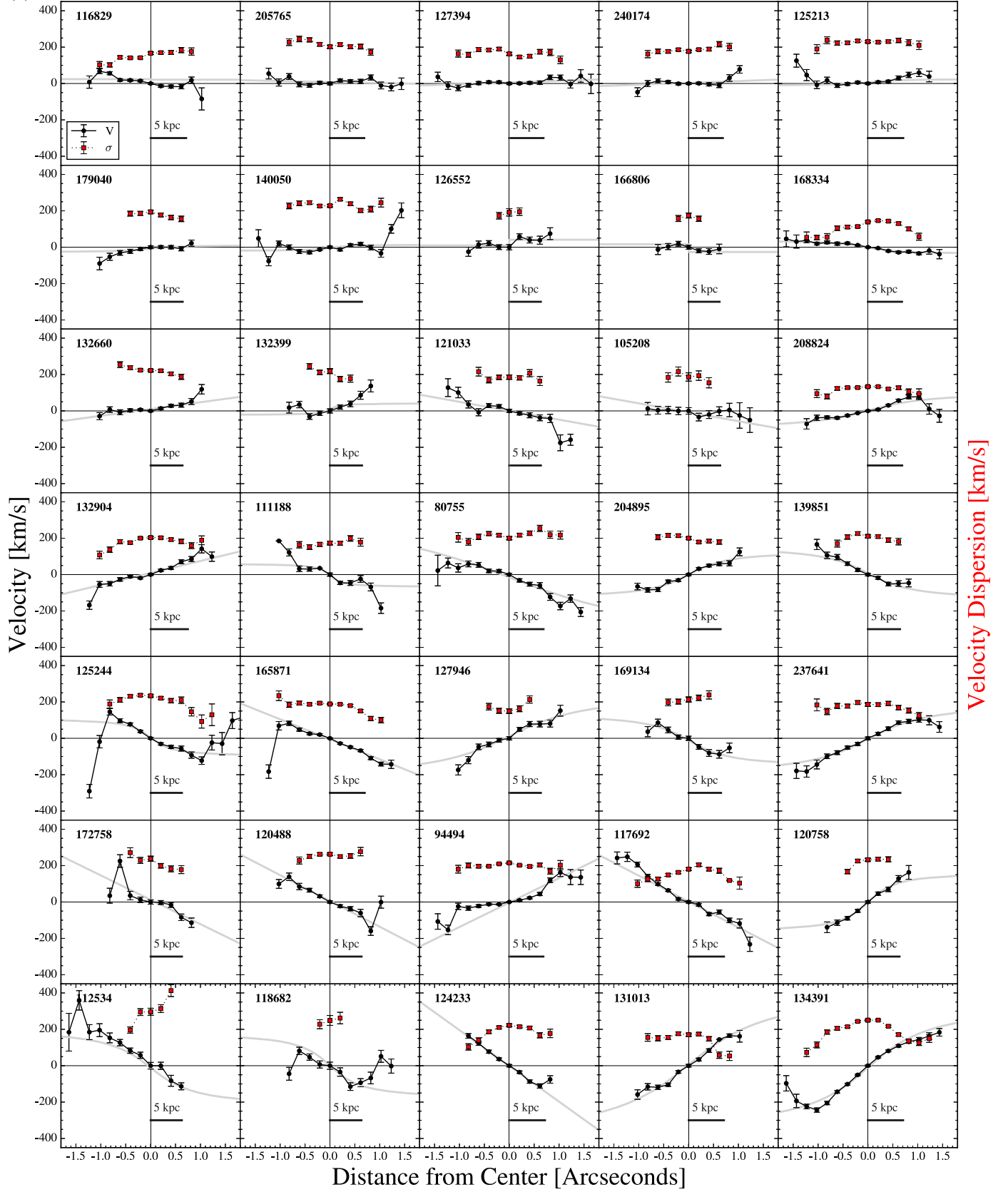
Figure 3. (Continued.)
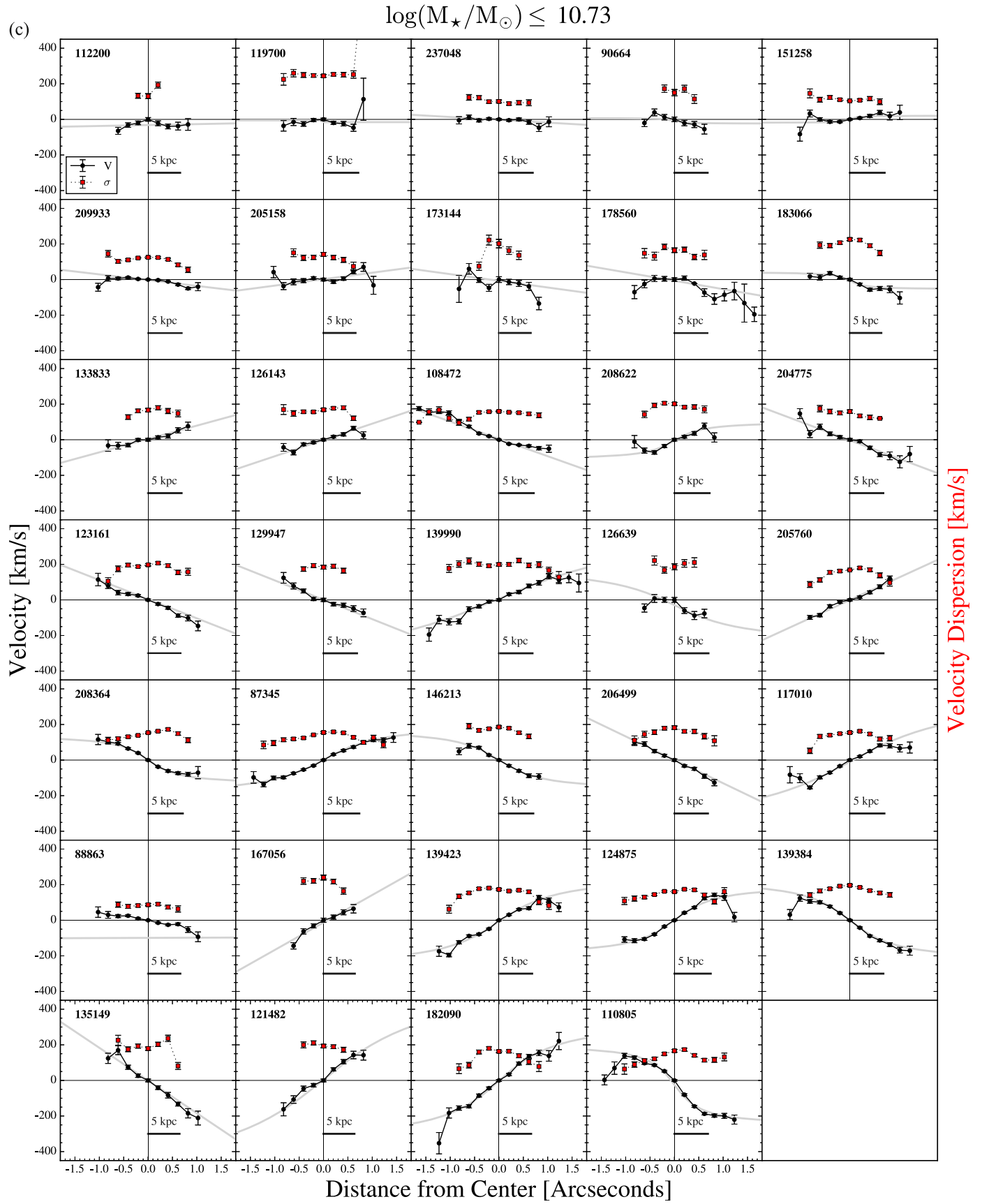
3. Stellar Rotation in Quiescent LEGA-C Galaxies

In this section, we investigate trends of stellar rotation and rotational support with other properties of massive quiescent galaxies. We specifically focus on stellar mass, with which rotational support has been demonstrated to depend in $z \sim 0$ galaxies, and on the two photometric measures that have been used to assess the "disk-like" nature of massive quiescent galaxies at high redshifts: projected axis ratio and Sérsic index (e.g., van der Wel et al. 2011; Chevance et al. 2012; Chang et al. 2013; Cappellari 2016; Graham et al. 2018). We note that the measured $|V|/\sigma$ will depend on projection effects, which is particularly important in interpreting trends in projected axis ratio. Therefore in addition to $|V_5|/\sigma_0$, we introduce $(V_5/\sigma_0)^*$ following, e.g., Binney (1978) and Davies et al. (1983), which is defined as the V/σ normalized by the $(V/\sigma)_O$ for an oblate, isotropic model and should be largely independent of projection effects. We adopt the approximation $V/\sigma \approx \sqrt{\epsilon/(1-\epsilon)}$ from Kormendy (1982) following this definition:

$$(V_5/\sigma_0)^* = \frac{(|V_5|/\sigma_0)}{\sqrt{\epsilon/(1-\epsilon)}}. \qquad (1)$$

Figure 4 shows rotational velocity (V_5) of galaxies in the top row, velocity dispersion in the second row, rotational support ($|V_5|/\sigma_0$) in the third row, and in the bottom row rotational support with a correction for projection effects, $(V_5/\sigma_0)^*$, as a function of stellar mass (left), projected axis ratio (center), and Sérsic index (right). Average uncertainties on the measurements are indicated by errorbars in the upper right corners of each panel. Running median and mean are indicated by red dashed and blue solid lines respectively for bins with greater than three data points. Errors on the mean are estimated in each bin via jackknife resampling. In each case these trends are best described as scatter between no rotational support and a maximum value that depends on the property plotted on the horizontal axis. This leads to measured (anti-)correlations, for which we quote the Pearson correlation coefficient in the upper left corner of each panel.

In the left panels, we see that more massive galaxies exhibit lower rotational support ($|V_5|/\sigma_0$ or $(V_5/\sigma_0)^*$) than less massive galaxies. This is also evident in the local universe (e.g., Emsellem et al. 2011). We will return to this trend in Figure 5, where we also include information about galaxy morphology in the same panel. We emphasize that this is primarily due to the known correlation between stellar mass and velocity dispersion, the mass Faber & Jackson (1976) relation (left panel, second row); rotational velocities alone do not exhibit a strong correlation with stellar mass (top left panel). However, at all masses there is at least a small fraction of galaxies that are observed to have very little rotational support. Some of this is an observational effect: beam smearing, inclination, and slit misalignment diminish ordered rotation and increase observed velocity dispersions and we expect this to preferentially impact smaller galaxies. We investigate these effects in greater detail in Section 4.2.

Another key result of our measurements is that galaxies that are flat in projection generally show rotation in their stellar body, whereas round galaxies do not (top center panel in Figure 4). This is well-understood as largely due to a combination of intrinsic elongation and projection effects (e.g., Cappellari et al. 2007; Emsellem et al. 2007, 2011;

Fogarty et al. 2014, 2015; van de Sande et al. 2017). This trend is tightened when rotational support is compared to dispersion support in the central pixel (third row, center panel in Figure 4), with a Pearson correlation coefficient $r = -0.41$. This is primarily a trend in rotational velocity, not velocity dispersion (see middle panel, second row). There is a subset of elongated galaxies that show little rotation (three of 25 galaxies with $b/a < 0.5$ have $|V_5|/\sigma_0 < 0.1$). The nature of these galaxies remains to be determined, but perhaps they are not unlike NGC 4550, which does not show net rotation but has been demonstrated to consist of two counter-rotating disks (Johnston et al. 2013). This overall trend implies that the distribution of projected axis ratios for a population of quiescent galaxies will be a decent estimate of the overall observed degree of rotational support. However, for any individual galaxy with an observed axis ratio of $b/a \gtrsim 0.6$ a significant fraction of galaxies will still have significant rotation and spatially resolved kinematics will be necessary to distinguish between pressure and rotationally supported systems.

Intriguingly, although both velocity (top right panel) and rotational support (third row, right panel) exhibit a statistically significant correlation with Sérsic index, the mean relation turns over exactly at the Sérsic index where one would expect the anti-correlation to be strongest. Although the numbers are small, the mean rotational velocity of galaxies that would be classified as disk-like based on their concentrations ($n < 2.5$) is not elevated ($\langle |V_5|/\sigma_0 \rangle = 0.33$, median $= 0.34$) compared to the overall average ($\langle |V_5|/\sigma_0 \rangle = 0.31$). This trend is strongest for the highest-mass quiescent galaxies ($\log M_\star/M_\odot > 11$), for which the $n < 2.5$ average $\langle |V_5|/\sigma_0 \rangle = 0.20$ versus overall $\langle |V_5|/\sigma_0 \rangle = 0.25$. These massive galaxies are the most extended, and therefore the least affected by beam smearing, and yet this trend is contrary to expectations. Larger samples, such as the full four year LEGA-C sample, will likely include a larger number of $n < 2.5$ galaxies and allow for a more statistically significant assessment of these trends. Regardless, we emphasize that measuring the Sérsic index of an individual quiescent galaxy cannot determine whether it is rotationally supported. Overall, Sérsic index is anti-correlated with rotational support, with a weaker Pearson coefficient $r = -0.41$.

Although measured $|V|/\sigma$ will likely be sensitive to projection effects, $(V_5/\sigma_0)^*$, which normalizes out expected V/σ based on projected axis ratios for an oblate, isotropic model, should be largely independent of projection effects. The bottom row of Figure 4 shows $(V_5/\sigma_0)^*$ as a function of stellar mass, projected axis ratio, and Sérsic index. Although all quantities are still correlated with this measure of rotational support, it is clear that a significant fraction of the correlation with projected axis ratio was covariance of the variables; once the projection effects are removed, the projected axis ratio exhibits a mild correlation with rotational support ($r = 0.25$). This remaining correlation is likely driven by the four round ($b/a > 0.8$) galaxies with high $(V_5/\sigma_0)^*$ that are not well approximated by isotropic oblate rotators. We note that, although inclination and projection effects can account for some of the anti-correlation between $|V_5|/\sigma_0$ and Sérsic index, the weak anti-correlation remains between $(V_5/\sigma_0)^*$ and Sérsic index. We reiterate that this sample includes very few low Sérsic index galaxies and, although we caution again the use of Sérsic index to characterize individual galaxies, we do not have the statistics to characterize this trend at low Sérsic indices.
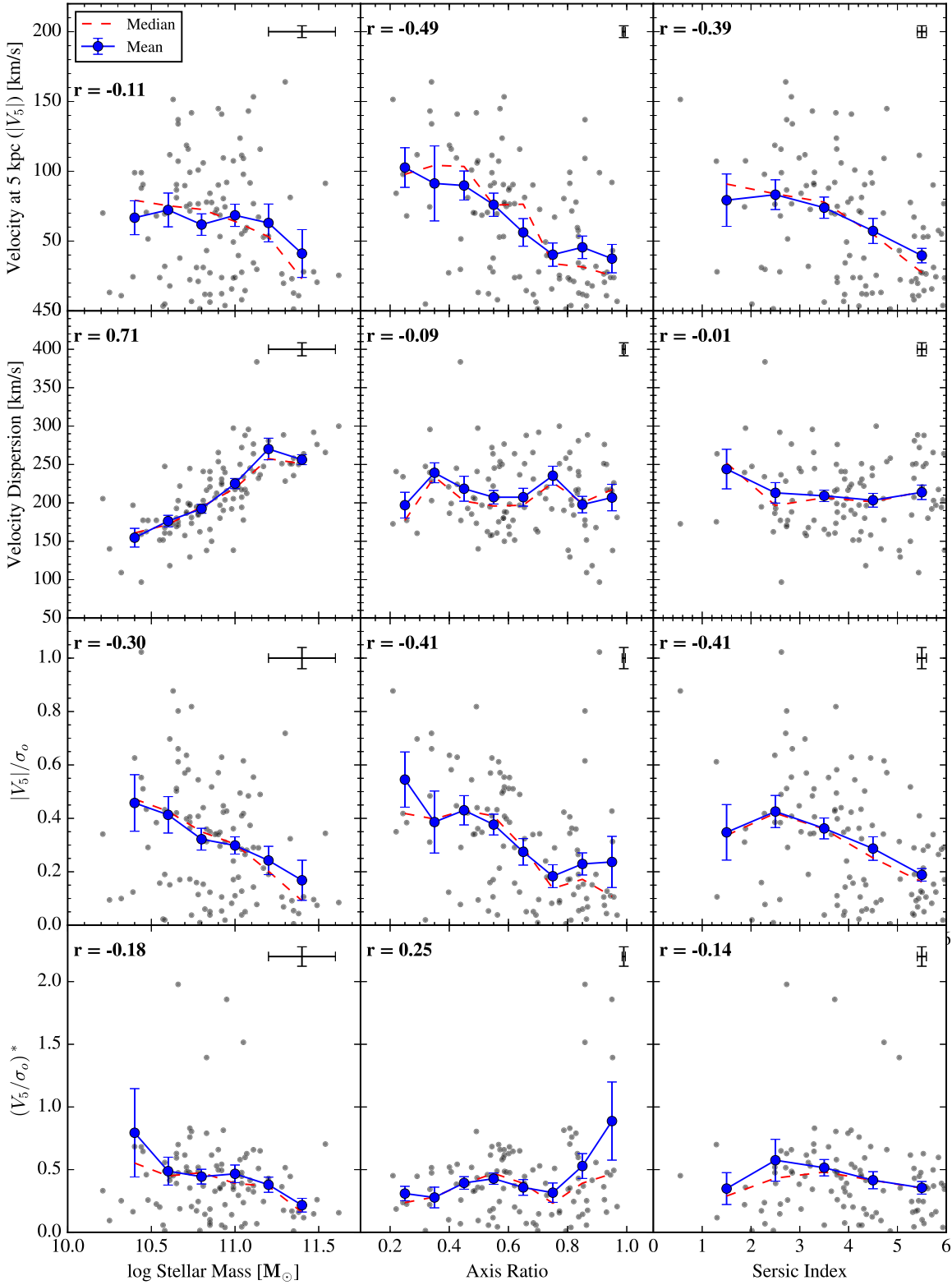
Figure 4. Rotational velocity ($|V_5|$, top row), central velocity dispersion (σ_0, second row), rotational support ($|V_5|/\sigma_0$, third row), and rotational support normalized by the expectation for an oblate rotator given the measured projected axis ratio ($(V_5/\sigma_0)^*$, bottom row) in quiescent LEGA-C galaxies vs. stellar mass (left), projected axis ratio (middle), and Sérsic index (right). Individual galaxies are indicated by small gray symbols; median and mean trends are indicated by red dashed and blue solid lines and symbols, respectively. The strongest correlation exists between stellar mass and velocity dispersion, or the "mass" Faber–Jackson relation. Projected axis ratio exhibits the strongest anti-correlation with $|V_5|/\sigma_0$ and, unlike the Sérsic index, the population average with $|V_5|/\sigma_0$ does not flatten out at elongated axis ratios in this sample. When projection effects are minimized with $(V_5/\sigma_0)^*$, this removes significant correlations with projected axis ratios, suggesting roughly similar correlations between rotational support and stellar mass, axis ratio, and Sérsic index.
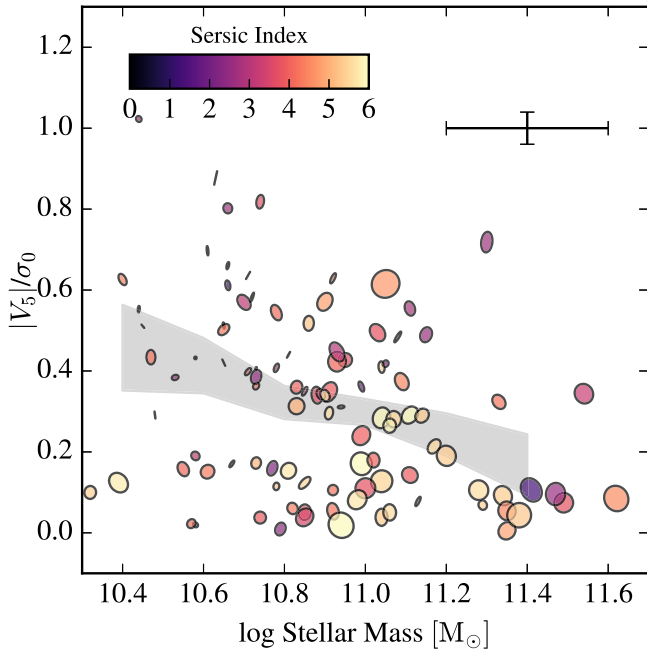
Figure 5. Rotational support ($|V_5|/\sigma_0$) vs. stellar mass for the LEGA-C sample of massive, quiescent galaxies. Symbol size indicates the galaxy effective radii (in log scale) and position angles and axis ratios of symbol ellipses reflect those of the galaxies. Symbol color indicates Sérsic index. The mean relation is indicated by the gray band and average uncertainty is indicated by errorbars in the upper right corner. The majority of high-mass galaxies have minimal rotational support, even when their Sérsic indices are disk-like; however, there are several high-mass galaxies with significant rotation. Below $\log M/M_\odot \lesssim$ 11.2 galaxies exhibit a range in rotational support and smaller and more elongated galaxies consistently show higher measured $|V_5|/\sigma_0$.

Figure 6. Observed rotational support of LEGA-C galaxies vs. stellar mass for star-forming (blue diamonds) and quiescent galaxies (red circles). Average uncertainties, shown as blue and red errorbars in the upper right, are higher for the star-forming galaxies ($\sim$0.1) than for quiescent galaxies ($\sim$0.04) in the LEGA-C sample. The right panel indicates the histograms in rotational support between the star-forming and quiescent populations; the distributions are overlapping but on average star-forming galaxies show higher V_5/σ_0 than quiescent galaxies overall and at fixed mass.

Figure 5 shows rotational support ($|V_5|/\sigma_0$) versus stellar mass, but now with symbols that reflect morphologies. Symbol sizes correspond to logarithmically scaled galaxy effective radii, and symbol axis ratios and position angles reflect the projected galaxy shapes and orientations. Symbol colors correspond to Sérsic index. The average uncertainty is indicated by the errorbars in the upper right and the mean trend, as calculated in Figure 4, is indicated by the gray band. Here we can clearly identify massive galaxies with seemingly inconsistent morphologies and measured kinematics: galaxies with little observed rotational support, but low Sérsic indices (purple colors) as well as others with high Sérsic indices (orange colors) and high $|V_5|/\sigma_0$.

Our measured $|V_5|/\sigma_0$ is likely to be an underestimate due to a number of observational effects such as rotational velocities contributing to central velocity dispersions and decreasing measured line-of-sight velocities due to inclination. Therefore, galaxies with low measured rotational support may in fact be revealed to be intrinsically fast rotators with full modeling; however, galaxies that are observed to be rotating quickly cannot be slow rotators. Given this observational ambiguity we refrain from using the terms "fast" and "slow" rotators, but return to quantifying the observational biases in the following section.

Our kinematic measure $|V_5|/\sigma_0$ is not directly comparable to the classifiers used for present-day galaxies as seeing, slit-misalignment, and other observational effects are not taken into account. However, the trends in Figure 4 are very similar to those observed for present-day galaxies (e.g., Emsellem et al. 2011), and we conclude that at all cosmic times since at least $z \sim 1$ the quiescent galaxy population consists of
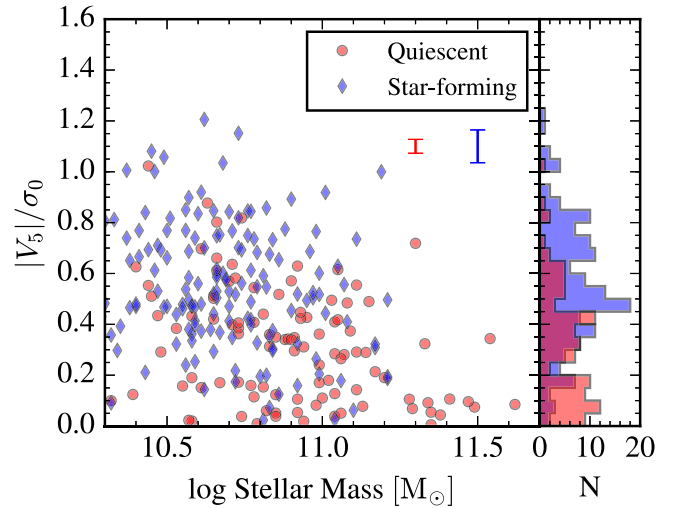
galaxies with low and high degrees of rotational support that reflect their intrinsic structure (spheroidal/triaxial and disk-like/oblate, respectively). At the same time, among the 10 most massive galaxies with stellar masses $>2 \times 10^{11} M_\odot$, only two show evidence for rotation. This is suggestive that the only way that galaxies can grow to such large masses is by a mechanism that reduces the angular momentum, that is, dissipationless merging. In the following section, we analyze the CALIFA data set to further explore the question of quantifying this evolution.

Although we focus on the quiescent sample only for this paper, we note that, as expected, the star-forming and quiescent galaxy populations differ in dynamics as well as stellar populations. Figure 6 shows the observed rotational support ($|V_5|/\sigma_0$) versus stellar mass for all galaxies with photometric axes within 45° of the N–S slits. Quiescent galaxies are indicated by red circles and star-forming galaxies by blue diamonds. The latter have more rotational velocity than the former, as found in the local universe (e.g., Cortese et al. 2016). Figure 1 demonstrates the known bimodality of these two populations in size and sSFR; this figure provides the first evidence for dynamical bimodality at high redshift based on stellar kinematics. The two populations overlap in observed phase space; however, their distributions differ significantly (see the histograms in the right panel). A two-sample Kolmogorov–Smirnov (K-S) test rejects the possibility that they are drawn from the same distribution with a $p = 1 \times 10^{-10}$, or $p = 4 \times 10^{-8}$ for massive $\log M_\star/M_\odot > 10.4$ galaxies. Average values of errors on V_5/σ_0 for the star-forming and quiescent sub-samples are indicated by blue and red errorbars in the upper right corner. Uncertainties in the $|V_5|/\sigma_0$ values, especially for the star-forming population, contribute significantly to the broadening of the distribution. Therefore, this discrepancy may be stronger in the intrinsic properties of the two populations. We leave the analysis of the dynamics of star-forming galaxies and of the joint population to future studies (C. Straatman et al. 2018, in preparation; J. van Houdt et al. 2018, in preparation).

4. CALIFA Stellar Kinematics and the Redshift Evolution of Rotational Support

The CALIFA survey provides an excellent census of the spectroscopic properties of local ($0.005 < z < 0.03$) galaxies of all morphological and spectral types (Sánchez et al. 2012; Walcher et al. 2014). The CALIFA team has promptly provided reduced data products in public data releases in addition to derived spectroscopic properties. For this project we include CALIFA galaxies from Data Release 3 (DR3, Sánchez et al. 2016), stellar kinematics maps from Falcón-Barroso et al. (2017), and spectroscopic classifications based on ionized gas lines from Cano-Díaz et al. (2016). Using this data set, we use intensity, stellar velocity, and stellar velocity dispersion fields in two spatial dimensions and extract profiles along a variety of axes and replicate the LEGA-C kinematic analysis on a local sample, quantifying intrinsic properties and simulating the effects of seeing on the measured LEGA-C rotation curves.

4.1. The CALIFA Data Set

Of the 667 galaxies in the full DR3, 300 are included in the Falcón-Barroso et al. (2017) analysis of stellar kinematics. This sample of galaxies, which have been observed with both low (V500) and medium (V1200) resolution gratings, is deemed to be representative of the full CALIFA sample in magnitude, size, and redshift, and spans a wide range of morphological types. As in the LEGA-C sample, Falcón-Barroso et al. (2017) remove strongly interacting galaxies from this kinematic sample. They analyze IFU datacubes for each galaxy, which are Voronoi binned to S/N $\sim$ 20 and the stellar kinematics are measured in each bin by fitting a combination of stellar templates convolved with a Gaussian line-of-sight velocity dispersion. These fits yield maps of velocity and velocity dispersion at each spaxel, which the authors provide on the CALIFA website (http://califa.caha.es/?q=content/science-dataproducts). They also provide stellar masses assuming a Chabrier (2003) IMF and effective radius, ellipticity, and position angle determined from the outer parts of the galaxies in SDSS imaging as described in Walcher et al. (2014).

We further limit our analysis to quiescent galaxies following the classifications of Cano-Díaz et al. (2016), who determine Hα-based SFRs and use ionized gas lines to differentiate among dominant ionization sources using EW(Hα) and the Kewley demarcation limit (Kewley et al. 2001) in the Baldwin–Philips–Terlevich diagram (Baldwin et al. 1981). Cano-Díaz et al. (2016) identify each CALIFA galaxy as either "Star-forming," "AGN," "Retired," or in ambiguous cases "Undefined." The Cano-Díaz et al. study include a representative sample of 535 galaxies that had been observed by 2015 February, and therefore does not completely overlap with the Falcón-Barroso et al. (2017) sample. We classify the remaining 10 galaxies by eye using the 2D star formation maps provided in the CALIFA DR3. For the most conservative comparison with the current study, we limit our analysis to the quiescent or Retired (EW(Hα) < 3 Å) sample of galaxies, based on their spectroscopic properties. Only four galaxies are classified as Retired by eye and we verify that excluding these does not significantly impact any of the conclusions in this paper. For maximum consistency in stellar population modeling, we compare stellar masses with those derived by Brinchmann et al. (2004) for the subset of these galaxies which also fall in the
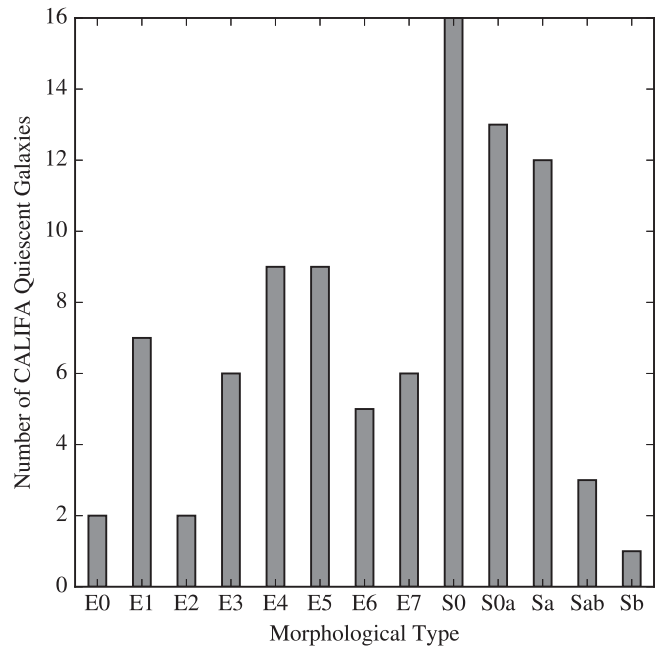

Figure 7. Morphological distribution of the 91 CALIFA galaxies determined to be quiescent based on EW(Hα) < 3 Å in the stellar kinematics sample.

spectroscopic SDSS DR7 sample. These fits are also based on aperture photometry and are analyzed using a similar methodology to our modeling of the UltraVISTA photometry. We find that CALIFA stellar masses are higher than those derived by Brinchmann et al. (2004) by a median of 0.16 dex for the retired galaxy population. We perform a linear regression to this subset and apply this correction to the CALIFA-derived stellar masses. The final sample includes 91 galaxies across a range of morphological types, from E0 to Sb as shown in Figure 7.

4.2. Simulating LEGA-C Observations with CALIFA Datacubes

For each galaxy in the quiescent CALIFA sample, we extract the intrinsic intensity $I_{1D}(x)$, velocity $V(x)$, and velocity dispersion $\sigma(x)$ profiles along lines passing through the maximum of the intensity map of the galaxy. These 1D profiles are measured along the published galaxy photometric position angles, as determined by Walcher et al. (2014) from galaxy outskirts in the SDSS imaging. Rotation curves are fit with arctangent functions and rotational velocity at 5 kpc and central velocity dispersion are measured as for the LEGA-C data set. These values correspond to the intrinsic V_5 and σ_0 values.

We use the 2D intensity and kinematic maps, spatially subsampled by a factor of 100, to simulate the observational effects of the misaligned $1''$ slits ($\sim$7.5 kpc), $0{''}205$ pixels ($\sim$1.5 kpc), and seeing characteristic of the LEGA-C observations. Slit misalignment in the LEGA-C survey, which in this study is limited to within 45° of the N–S slits, is simulated by extracting 1D profiles along the closer of the horizontal or vertical directions. The intensity in 2D position–velocity space can be defined as

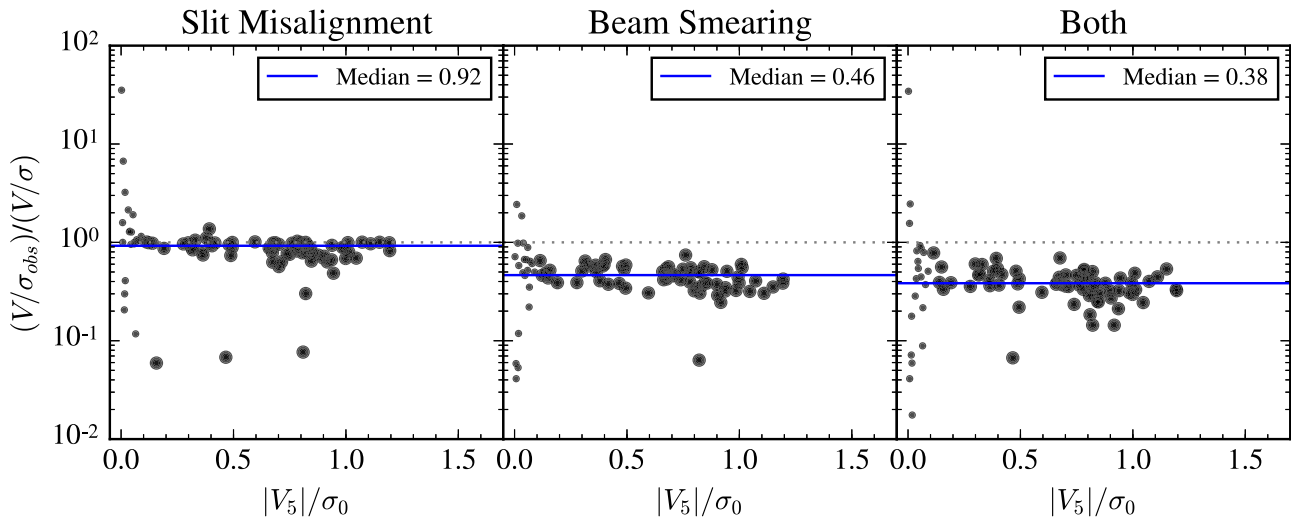$$I_{3D}(x, y, v) = I_{2D}(x, y)\exp\left[-\frac{(v - V(x, y))^2}{2\sigma(x, y)^2}\right]. \qquad (2)$$

13

Figure 8. Ratio of simulated "observed" to intrinsic rotational support ($|V_5|/\sigma_0$) vs. the intrinsic value due to slit misalignment (left panel), beam smearing (center panel), and the combined effects (right panel). Galaxies with minimal rotational support ($|V_5|/\sigma_0 < 0.1$) are indicated by small symbols and those with higher $|V_5|/\sigma_0$ by large symbols. Beam smearing is the dominant effect, decreasing the observed $|V_5|/\sigma_0$ by a median factor of ~2.2, while slit misalignment decreases the value by $\sim8\%$.

The effects of seeing are then simulated by convolving this intensity (I_{3D}) field with a 2D Moffat profile. For this we adopt a uniform value of $FWHM_{PSF} = 7$ kpc as representative of the LEGA-C redshift and spectrum (FWHM $\sim 1''0$ at the average $z = 0.78$). We adopt a value of $\beta = 4.765$ following Trujillo et al. (2001). The velocity and velocity dispersion profiles are then measured as the intensity-weighted first and second moments of $I_{3D}(x, y, v)$, summed within a 7.5 kpc band perpendicular to the horizontal or vertical slit and within 1.5 kpc pixels along the slit. These profiles are measured from the initial and convolved intensity fields. The "observed" rotational velocity (V_5) and central velocity dispersion (σ_0) are measured as in the LEGA-C data set. The resulting intrinsic and binned unconvolved and convolved rotation curves and velocity dispersion profiles of the CALIFA galaxies are included in Figure 14 in Appendix A.

Figure 8 shows the ratio of simulated "observed" $|V_5|/\sigma_0$ to the intrinsic value for the two main effects included in the simulation, slit misalignment (left panel) and beam smearing (center panel), and for the combination versus the intrinsic value measured along the position angle (right panel). In each panel the median value is indicated by a horizontal blue line. Overall, the impact of slit misalignment and beam smearing from the simulated PSF ($FWHM_{PSF} = 7$ kpc) on the measured rotation curves is significant, with the latter dominating the difference from the intrinsic and blurred 1D rotation curves. Slit misalignment decreases the measured ratio by an average of $\sim8\%$. Straatman et al. (2017) found the impact of slit misalignment to be stronger for emission line galaxies, finding that this effect decreases the measured velocities by a median factor of 1.19 with significant scatter. However, we note that those simulations were for a very different sample of galaxies and were produced using infinitely thin galaxy models. It may be the case that at $z \sim 1$ the LEGA-C quiescent galaxies are more disk-like than quiescent galaxies in CALIFA (e.g., Chang et al. 2013); however, these galaxies will likely be either triaxial or oblate spheroids and not well described by thin disk

models. These models would overpredict the effect of slit misalignment for a sample with likely non-zero minor axis rotation.

The second effect of beam smearing (center panel) is driven by differences in the measured rotational velocity as ordered motion contributes to velocity dispersion in the outer parts of the simulated galaxies. The measured $|V_5|/\sigma_0$ decreases by an average factor of ~2.5 after convolution with a 7 kpc point spread function (PSF), and this effect would only increase with a larger PSF. Although beam smearing significantly changes the velocity dispersion profiles, it only minimally influences the measured central velocity dispersion, with a median ratio of observed velocity dispersion to intrinsic of 0.98 and in all cases it is less than a $\sim10\%$ effect. Therefore the diminished $|V_5|/\sigma_0$ in Figure 8 is primarily due to the lowered $|V_5|$.

Beam smearing impacts smaller galaxies more severely than large galaxies, as shown in Figure 9. This figure shows the ratio of simulated to intrinsic $|V_5|/\sigma_0$ versus galaxy stellar mass and size in the CALIFA sample. In each panel the running average is indicated by the blue dashed line for the full sample and the red solid line for galaxies with $|V_5|/\sigma_0 > 0.1$, for which uncertainties are measured via jackknife resampling. Measured rotational support will be reduced by nearly an order of magnitude for the lowest mass and smallest galaxies in the sample, whereas the largest and most massive galaxies are less impacted by these simulations. These trends suggest that the differential effect corresponds to a factor of ~2 difference between $\log M/M_\odot \sim 10.4$ and $\log M/M_\odot \sim 11.4$ or $R_e \sim 1$ kpc and $R_e \sim 10$ kpc.

The overall effects of beam-smearing and misalignment are presented in Figure 10, which shows $|V_5|/\sigma_0$ versus stellar mass. Black stars indicate the intrinsic values along the photometric axis, connected by black dashed lines to blue circles from the simulations. The PSF preferentially decreases the observed rotation in lower mass galaxies. Furthermore, these observational effects lower the observed range in $|V_5|/\sigma_0$, thereby diminishing the dichotomy between slow and fast rotating galaxies. Although the intrinsic $|V_5|/\sigma_0$
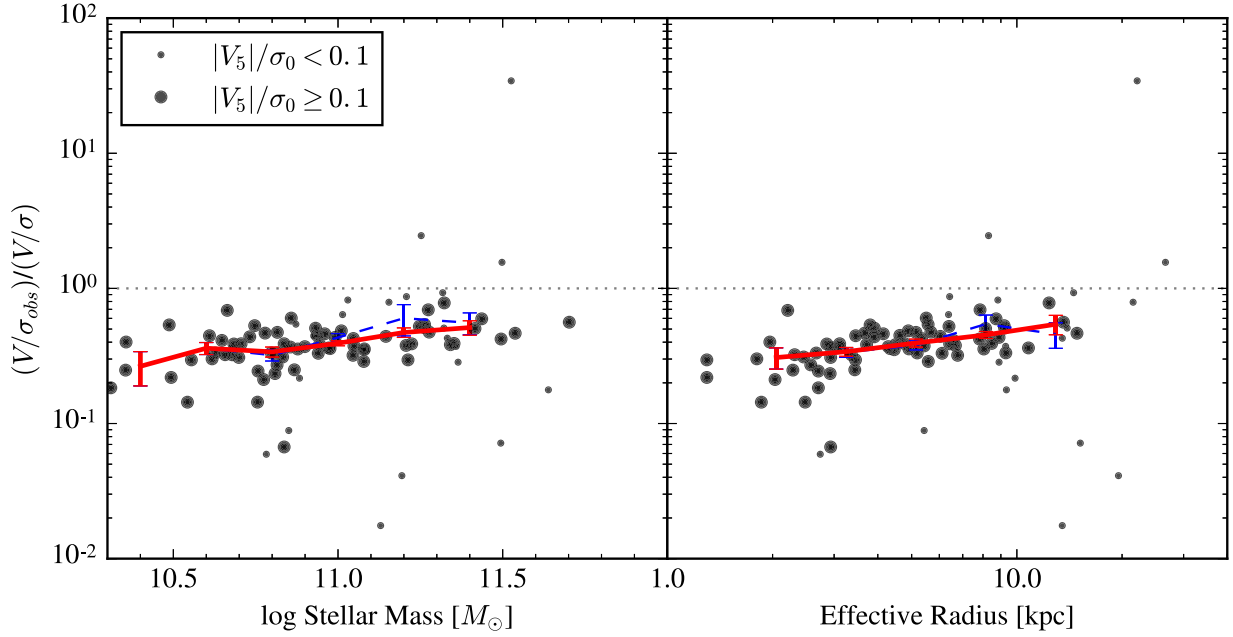
Figure 9. Trends in the ratio of observed to intrinsic $|V_5|/\sigma_0$ from the CALIFA simulations with stellar mass in the left panel and effective radius in the right panel. Small symbols indicate galaxies with $|V_5|/\sigma_0 < 0.1$, which are most sensitive to this relative metric. The running mean relations are indicated by blue dashed (all galaxies) and red solid ($|V_5|/\sigma_0 > 0.1$) lines. As expected, the blurred rotational support preferentially impacts the least massive and most compact galaxies because of the relative size of the PSF and the galaxy extent.
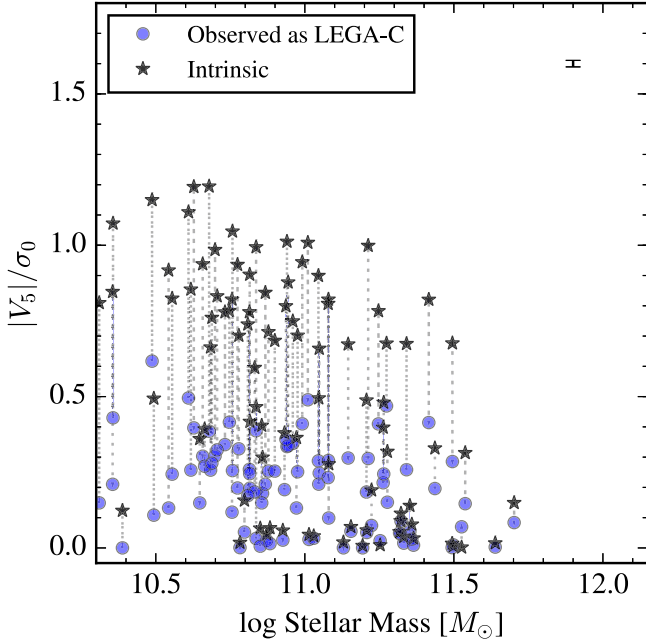
Figure 10. Rotational support ($|V_5|/\sigma_0$) vs. stellar mass of CALIFA galaxies. The intrinsic values, as measured along the photometric position angle, are indicated by black stars. The average uncertainty in this measurement is indicated by the black errorbar in the upper right corner. The $|V_5|/\sigma_0$ for each galaxy with a misaligned slit and after convolution with a Moffat PSF (FWHM$_{\rm PSF}$ = 7 kpc) is indicated by a blue circle, with measurements for each galaxy connected by gray dotted lines. Because the simulated PSF is significant relative to the physical extent of galaxies, the measured rotational support is strongly affected by the observational effects.

measurements extend to much higher values (>1.0), all simulated $|V_5|/\sigma_0$ values are below 0.5 and the correlation between stellar mass and rotational support is all but erased.

4.3. Measuring Redshift Evolution

Armed with the CALIFA sample of $z \sim 0$ galaxies for which we have similar measurements of rotational support and have simulated the observational effects that are impacting the LEGA-C observations, we now turn to assess the redshift evolution of the rotational support of quiescent galaxies. Before comparing the two samples, we would like to verify that they span similar regions of parameter space. In Figure 11 we show the distributions of the CALIFA and LEGA-C quiescent samples in stellar mass (left panel), projected axis ratio (center panel), and central velocity dispersion (right panel). In each case we perform a two-sample K-S test to evaluate whether the two samples are likely to be drawn from the same distributions. The K-S tests suggest that the samples are very well matched in projected axis ratio and velocity dispersion, while the stellar mass distributions are slightly different, with a p-value of 0.088, but not at a statistically significant (e.g., 3σ) level. We emphasize that stellar masses are extremely sensitive to differences in modeling of the photometry and the stellar populations, whereas the other two properties (b/a and σ_0) are measured reasonably consistently between the two samples and are generally less sensitive to systematics. In particular, we note that this difference also complicates comparisons between the two samples at fixed mass. We conclude that the CALIFA and LEGA-C samples are reasonably well-matched in axis ratio distribution and gravitational potentials to test redshift evolution of $|V|/\sigma$.

Figure 12 shows the rotational support versus stellar mass for the simulated "observed" CALIFA galaxies at $z \sim 0$ in the left panel (gray symbols, blue dashed line), the LEGA-C sample at $z \sim 0.8$ in the center (black diamonds, black solid line), with the running averages on the individual panels and together on the right panel. Uncertainties in the averages are calculated using jackknife resampling. For these comparisons we use
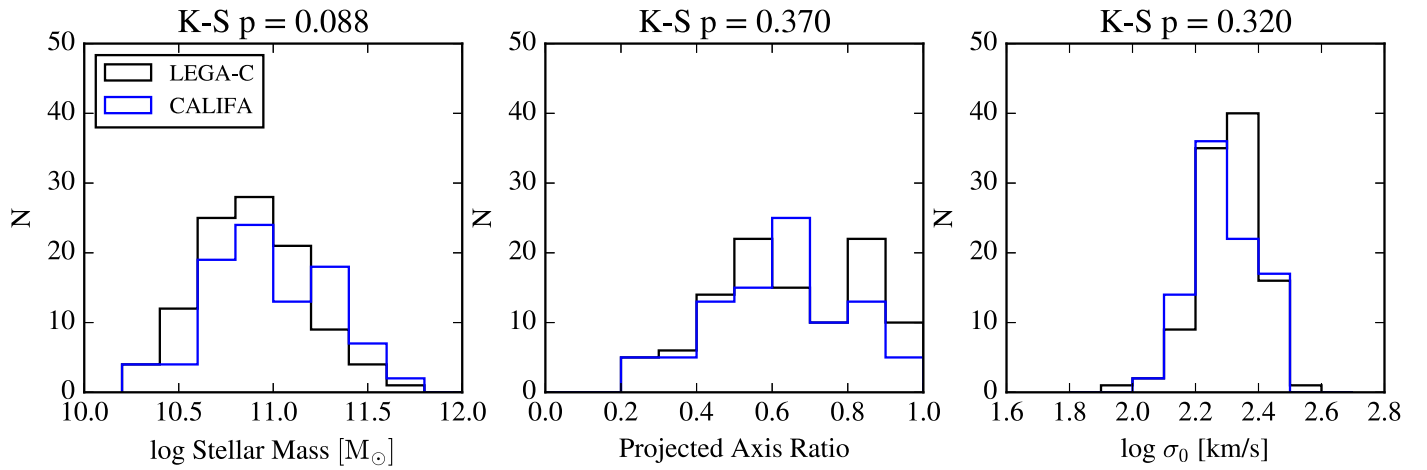
Figure 11. Distributions of LEGA-C (black) and CALIFA (blue) data sets in stellar mass (left panel), projected axis ratio (center panel), and velocity dispersions (right panel). The p-value of a two-sample K-S test is indicated at the top of each panel. Although the stellar mass distributions are not consistent at the 10% level between the two samples, this property is sensitive to subtle differences in the modeling of the stellar populations between them. The projected axis ratio and velocity dispersions are consistent with being drawn from the same distributions between the two surveys, with $p = 37\%$ and $p = 32\%$ respectively.

$(V_5/\sigma_0)^*$ as a measure of rotational support to minimize scatter introduced by projection effects.

Below $\log M_\star/M_\odot \sim 11.25$ galaxies at high redshift exhibit slightly ($\sim 50\%$) more rotational support than those in the CALIFA sample. At the highest masses, the two samples are nearly consistent within the measurement uncertainties. However, the structural evolution of massive galaxies (e.g., Bezanson et al. 2009; Hopkins et al. 2009; Naab et al. 2009; van Dokkum et al. 2010) and evolution of the stellar mass function (e.g., Muzzin et al. 2013b) imply that galaxies must grow in mass through cosmic time. Therefore, evolution at fixed mass is likely an underestimate in the dynamical evolution of individual galaxies. Empirically motivated work (e.g., Leja et al. 2013; Patel et al. 2013; van Dokkum et al. 2013) and theoretical studies (Behroozi et al. 2013; Torrey et al. 2015, 2017) have estimated mass growth rates of ~ 0.15 dex for massive LEGA-C-like galaxies since $z \sim 1$. Accounting for this would imply stronger evolution than the comparison at fixed mass (red dashed line in Figure 12).

Another option is to compare at fixed central velocity dispersion, which may be a more stable property for an evolving galaxy (Oser et al. 2011; Bezanson et al. 2012; van de Sande et al. 2013; Belli et al. 2014a, 2014b). We note that the effects of beam smearing can influence the measured central velocity dispersions; however, from our simulations of the CALIFA stellar kinematics we expect this to be at most a few percent effect. Figure 13 follows the same conventions as Figure 12, but now compares rotational support to central velocity dispersion (σ_0). This also has the benefit of avoiding inconsistencies between samples in the stellar population synthesis (SPS) modeling used to estimate stellar mass. These panels indicate that, for all galaxies at fixed velocity dispersion, rotational velocities are $\sim 50\%$–100% higher at $z \sim 0.8$ than in local quiescent galaxies, with an average ratio of 1.94 ± 0.22. Qualitatively, the observed evolution in rotational support at fixed velocity dispersion is robust to aperture and size evolution. In Appendix B we investigate the use of two additional apertures. First, we adopt an aperture that scales with the average effective radius, comparing rotation within 7.5 kpc for the CALIFA data set at $z \sim 0$ with $(V_5/\sigma_0)^*$ for the LEGA-C

sample. Although the apparent evolution in rotational support is weaker than within a fixed aperture, with an average ratio of $\langle (V_5/\sigma_0)^*_{z=0.8}/(V_{7.5}/\sigma_0)^*_{z=0} \rangle = 1.41 \pm 0.16$. This difference, significant at only the $\sim 95\%$ level, is consistent with the results obtained using a more robust fixed aperture, and paint a similar picture that the degree of rotational support is higher than at the present day. We also test the use of the maximum observed velocities (V_{max}) measured from each rotation curve, defined as the value of the best-fit arctangent function at the maximum extent, averaged symmetrically. This comparison yields an evolution of $\langle (V_{max}/\sigma_0)^*_{z=0.8}/(V_{max}/\sigma_0)^*_{z=0} \rangle = 1.76 \pm 0.22$, which is consistent with the evolution within 5 kpc at the $\sim 1\sigma$ level.

These results suggest a significant evolution in the rotational support of quiescent galaxies. At face value, this is consistent with results from the Chang et al. (2013) study, which found a decrease in the fraction of oblate rotators in massive ($10.8 < M_\star/M_\odot < 11.5$) quiescent galaxies from CANDELS/3DHST at $1 < z < 2.5$ to SDSS at $z \sim 0.06$. Although the statistics in the study are somewhat small, they found a factor of ~ 2–4 increase in the oblate fraction between SDSS and $0.6 < z < 0.8$ and $0.8 < z < 1.3$. However, this study also found no statistically significant evolution in the fraction of oblate rotators in the intermediate mass ($10.5 < M_\star/M_\odot < 10.8$), where we observe an evolution in the $|V_5|/\sigma_0$ at fixed mass.

We note here that there are subtle differences between the CALIFA and LEGA-C samples. Although we do not expect any to dominate the conclusions of this study, we mention them now for completeness. First, the distinction between quiescent and star-forming galaxies is defined differently for each sample: CALIFA uses spectroscopic criteria whereas for LEGA-C we use photometric colors. Second, although both surveys are initially magnitude limited, the CALIFA data set is selected with an additional angular size selection to optimally utilize the IFU spectrograph. This latter selection will bias the CALIFA data set against small galaxies and in particular will render the sample incomplete at the low-mass end; however, we note that at $9.7 < \log M_\star/M_\odot < 11.4$ the overall CALIFA sample is representative in size (Walcher
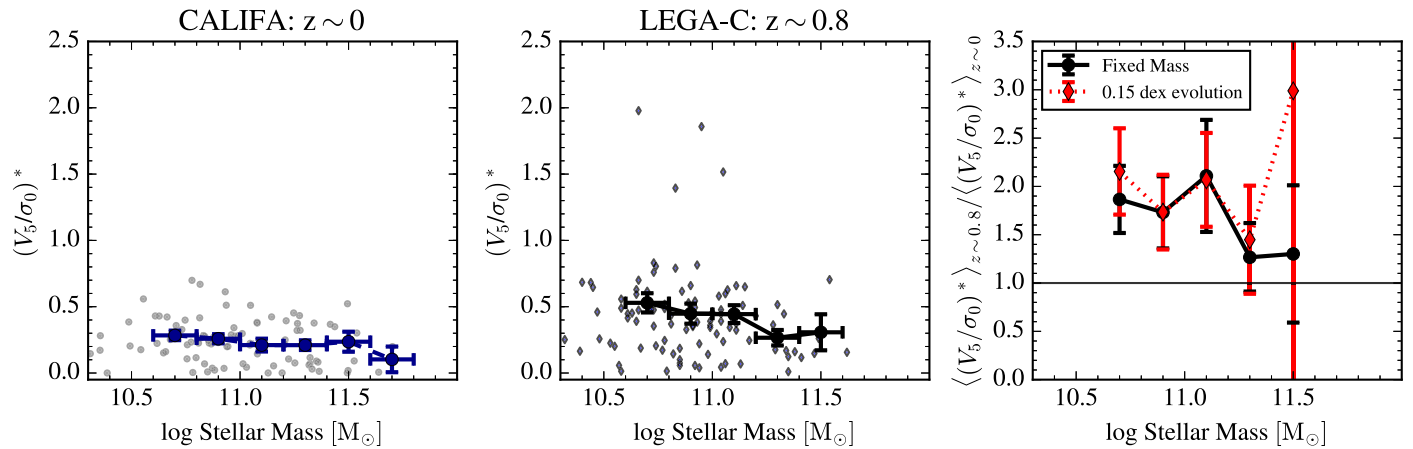
Figure 12. Rotational support ($(V_5/\sigma_0)^*$) vs. stellar mass for the simulated CALIFA $z \sim 0$ galaxies (left panel), LEGA-C galaxies at $z \sim 0.8$ (center panel), and the ratio of the averages (right panel). At the highest-mass end ($\log M_\star/M_\odot \gtrsim 11.25$) the rotational support is very similar, but at lower masses, the LEGA-C sample exhibits similar or slightly more rotational support than CALIFA galaxies at fixed mass (black symbols and solid line in the right panel). However, when compared to more massive descendants (red symbols and dashed line, assuming 0.15 dex evolution) galaxies at $z \sim 0.8$ exhibit 50%–100% higher rotational support than local galaxies.

et al. 2014), which safely includes the current sample. Furthermore, only 300 (∼80%) of the CALIFA DR3 galaxies with V1200 grating data are included in the Falcón-Barroso et al. (2017) stellar kinematics sample. Although the authors emphasize the representative redshifts, sizes, and absolute magnitudes of the resulting sample with respect to the full CALIFA data set, the 75 galaxies that are eliminated due to poor quality stellar kinematic maps could introduce additional bias in the kinematic properties of quiescent galaxies. Finally, we have not attempted to match the LEGA-C and CALIFA samples in volume or environment or explicitly link individual progenitor and descendant galaxies. While we note that this could strengthen our conclusions about the redshift evolution of the dynamical structures of quiescent galaxies, it is beyond the scope of this paper.

5. Discussion and Conclusions

In this paper, we present the first results from spatially resolved stellar kinematics of a large sample of massive, quiescent galaxies at large lookback time, drawn from ESO's Public Spectroscopic LEGA-C Survey. As opposed to earlier work on smaller samples (Moran et al. 2007; van der Marel & van Dokkum 2007; van der Wel & van der Marel 2008) our sample is not selected on the basis of visual morphology, but rather by a lack of star formation, preventing a possible bias against disk-like, passive galaxies. The exceptional depth of the LEGA-C spectroscopic survey allows for spatially resolved kinematic modeling of the continuum beyond two effective radii of galaxies at $z \sim 1$.

We have demonstrated that galaxies at $z \sim 0.8$ follow a similar trend of decreasing rotational support with increasing stellar mass as local early-type galaxies (e.g., Cappellari et al. 2007; Emsellem et al. 2011). But also like their local counterparts (e.g., Veale et al. 2017), there exist examples of very massive fast-rotators in the LEGA-C sample. We find that ∼90% of very elongated galaxies, with projected axis ratios less than ∼0.6, exhibit significant rotation. The latter result adds credence to the empirical result that massive galaxies at high redshifts are more disk-like based on axis ratio

distributions (e.g., Chang et al. 2013). Conversely, the lack of a clear trend between rotation and Sérsic index suggests that the concentration of a galaxy's light distribution is not a strong test of whether it is disk-like for quiescent galaxies. Furthermore, we emphasize that none of the properties (stellar mass, projected axis ratio, and Sérsic index) explored in this work definitively predicts the rotational support of an individual galaxy.

At fixed stellar velocity dispersion quiescent galaxies show ∼90% more rotation on average within an aperture of radius 5 kpc at $z \sim 1$ than in the present-day universe. The most plausible interpretation is that such galaxies have lost angular momentum over the past 7 Gyr. Further interpretation of this observation in terms of evolution of individual galaxies is complicated by the fact that a significant number of galaxies cease star formation and join the quiescent population between $z \sim 1$ and the present. This "progenitor bias" (e.g., Franx & van Dokkum 1996; van Dokkum et al. 2000) forces us to consider that star-forming galaxies show a larger degree of rotational support than quiescent galaxies of the same mass or velocity dispersion. Hence, we can firmly rule out the scenario that the cessation of star formation and the subsequent phase of evolution do not affect the dynamical structure: if that were the case, then we would see more rotational support among present-day quiescent galaxies compared to $z \sim 1$, instead of less.

There are two (extreme) scenarios to explain the observed evolution in the $|V_5|/\sigma_0$ distribution at fixed mass and velocity dispersion (Figures 12 and 13). A first scenario is that galaxies drastically and suddenly lose their net angular momentum concurrently with the cessation of star formation. In this case, individual quiescent galaxies would not need to lose angular momentum afterward to fit within the quiescent population. A second scenario is that angular momentum does not change in association with the cessation of star formation, and that quiescent galaxies gradually lose angular momentum through subsequent assembly, that is, dissipationless merging. In this scenario fast-rotating quiescent galaxies would be younger than slow-rotating galaxies. The reality might well be a mixture of these scenarios.
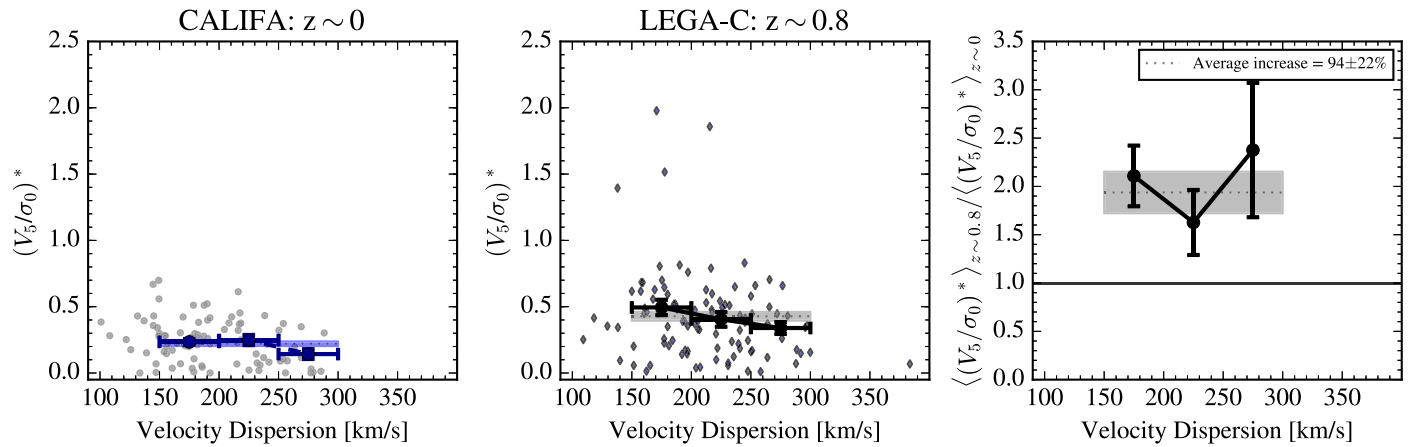
Figure 13. Rotational support ($(V_5/\sigma_0)^*$) vs. central velocity dispersion (σ_0) for the simulated CALIFA $z \sim 0$ galaxies (left panel), LEGA-C galaxies at $z \sim 0.8$ (center panel), and the ratio of the averages (right panel). In each panel individual galaxies are indicated by small symbols, larger black circles indicate the running averages and jackknife uncertainties, and the horizontal bands indicate the average value and uncertainty evaluated between $150 < \sigma < 300$ km s^{-1}. At fixed central velocity dispersion, which is likely more stable than stellar mass, the higher-redshift galaxies exhibit more rotational support than their local counterparts by a factor of $\sim$1.5–2.

A follow-up study with the larger LEGA-C sample will explore these scenarios by comparing dynamical structure with stellar population ages.

At this time we can already surmise that the first scenario—invoking rapid dynamical evolution—appears unlikely to be the dominant mode of evolution. Only major mergers can accomplish sudden and drastic changes in dynamical structure (e.g., Naab et al. 2014 and references therein) and few are seen among the star-forming population (e.g., Lotz et al. 2011; Man et al. 2016). This mode of transformation is not firmly ruled out, however, as the timescales used to translate between pair fractions or disturbed morphologies and merger rates remain somewhat uncertain. Given that merging timescales are short, if all galaxies that were to become quiescent via mergers, the merger fraction implied is potentially close to the observed one (e.g., Bell et al. 2006; Robaina et al. 2010). The second scenario—gradual loss of angular momentum—and the observed decline in the number density of very compact galaxies (Trujillo et al. 2009; Taylor et al. 2010) provide mutual support for dissipationless growth of quiescent galaxies.

Previous studies with morphologically selected galaxies have found contradictory results. van der Wel & van der Marel (2008) found no evidence for evolution in the rotational support of 25 $z \sim 1$ elliptical and S0 galaxies using Jeans modeling to determine intrinsic rotational velocities and velocity dispersion profiles under the assumption that mass-follows-light and axisymmetric orbits. However, using a similar analysis, van der Marel & van Dokkum (2007) found an increase in rotation rates of cluster elliptical galaxies at $z \sim 0.5$ at a confidence level of $\sim$90%. Our analysis is consistent with the van der Marel & van Dokkum (2007) study; however, we note several key differences that prevent a direct quantitative comparison of our results to the previous work. First of all, we do not attempt to derive intrinsic, yet model-dependent, properties of the galaxies in the LEGA-C sample. Instead, we self-consistently simulate the observational effects of seeing, slit geometry, and binning on our low-redshift sample. One of the possible explanations cited for the discrepancies between the two previous studies is

the different treatment of morphological classifications and potential misclassification of S0 galaxies in the van der Marel & van Dokkum (2007) study. In contrast, in this study we do not distinguish among morphological classes of galaxies: all galaxies with quenched star formation will fall into the high- and low-redshift samples, somewhat eliminating such progenitor biases. Of course one cannot avoid the bias introduced by excluding galaxies that are still forming stars.

Belli et al. (2017) found an evolution in the dynamical to stellar mass ratios versus axis ratios of disky quiescent galaxies, as defined by their Sérsic indices. They concluded that this difference implies an evolution in the average rotational support from $z \sim 1.5$–2.5 until $z \sim 0$, with the characteristic $|V|/\sigma$ decreasing from $\sim$3 to $\sim$1.5. This result is qualitatively consistent with our observed evolution given that the Belli et al. (2017) sample is at higher redshifts than the LEGA-C sample. However, we note that we find Sérsic index to be a very poor predictor of V/σ, especially at disk-like ($n < 2.5$) values.

Our result is consistent with predictions from simulations of isolated galaxy mergers (e.g., Wuyts et al. 2010), the remnants of which have higher V/σ at fixed ellipticities than local galaxies. Semi-analytic models constructed to explain the formation of fast- and slow-rotating early-type galaxies in the ATLAS3D sample predict strong evolution in the number densities of fast and slow rotators with time, implying an increase by 0.7 dex in the number density of slow-rotating galaxies and 0.2 dex for fast rotators since $z \sim 1$ for massive galaxies $\log M_*/M_\odot > 11$ (Khochfar et al. 2011). Furthermore, a smooth evolution of rotational support is apparent within the Illustris cosmological simulation for massive galaxies that exhibit little rotation at $z \sim 0$ (Genel et al. 2015). In this and other simulations (e.g., Naab et al. 2014), this evolution is due to a sequence of substantial minor merging. In this scenario, even rapidly rotating galaxies can evolve through time to slow rotators, highlighting the importance of our approach of not excluding galaxies that would be morphologically classified as late types in our comparison.

The current analysis falls short of deriving intrinsic dynamics for individual galaxies. Joint modeling of the spatially resolved kinematics and *HST*/ACS imaging including Jeans modeling, and assessment of the PSF size for each individual galaxy, to derive intrinsic properties would allow for a different direct comparison of the resolved kinematics of LEGA-C galaxies to local fast- and slow-rotating elliptical galaxies. This modeling is outside of the scope of the current paper, but is underway. Furthermore, this sample is only based on the first year LEGA-C data. Over the next few years, the full survey will be completed and the sample will increase by a factor of ∼4. Uncertainties in this kinematic modeling could be assessed by observing a subset of the current sample of galaxies with a perpendicular slit (E–W).

We have not addressed the question of whether rotational support depends on how recently a galaxy has quenched its star formation. If rotation is diminished via minor merging, one might expect to see differences in the stellar ages or metallicities between slow and strongly rotating galaxies. Furthermore, we have not investigated evolution within the ∼2 Gyr probed by the $0.6 < z < 1$ LEGA-C redshift range. Performing these tests while holding constant other properties that correlate with rotation would be difficult with the current sample of ∼100 LEGA-C galaxies. However, with the complete data set we will test correlated trends in stellar age, rotational support, size, and stellar mass to test whether newer additions to the red sequence exhibit predicted differences from their older counterparts.

Ideally, one would like to observe the rotational support of quiescent galaxies as close to their epoch of transformation as possible. Below $\log M_\star/M_\odot \lesssim 11$, where we expect galaxies to continue to grow and evolve below $z \sim 1$, the LEGA-C data set will probe stellar kinematics for star-forming progenitors and quiescent galaxies alike, in addition to any observable intermediate stages. For the most massive galaxies, we expect this to be at a much earlier epoch at $z \sim 2$–4 from either stellar ages and colors (e.g., Kriek et al. 2008; Whitaker et al. 2012a; McDermid et al. 2015; Glazebrook et al. 2017). However, at these redshifts continuum spectroscopy is extremely difficult, even with the latest-generation ground-based Near-IR spectrographs. Spatially resolving the stellar continuum has only been possible for a few strongly lensed quiescent galaxies (A. B. Newman et al. 2015, 2018, in preparation; Toft et al. 2017); unfortunately the low number density of massive quiescent galaxies will always render such targets extremely rare. The best hope for obtaining spatially resolved stellar kinematics in the near future is via deep spectroscopy with NIRSPEC on the *James Webb Space Telescope* or with adaptive-optics-assisted observations on 30 m class telescopes.

Appendix A
CALIFA 1D Rotation and Velocity Dispersion Profiles

In this section we provide the 1D profiles derived from the CALIFA stellar kinematics data cubes (Falcón-Barroso et al. 2017), as described in Section 4. All line-of-sight velocity and velocity dispersion profiles are included in Figure 14, split into three pages in bins of descending mass and ordered by increasing rotational velocity at 5 kpc, $|V_5|$. The 1D profiles are extracted both along the position angle derived from the SDSS imaging in the galaxy outskirts (Walcher et al. 2014) and along the closer of the horizontal or vertical axes to approximate the LEGA-C N–S slit positions and position angle threshold for the analysis in this paper. The profiles are included for all 91 retired CALIFA galaxies in Figure 14. The quantities determined along the misaligned slit are indicated by black (velocity) and red (velocity dispersion) symbols. The rotation curve is fit with an arctangent function and this fit is indicated by a black solid line. The velocity dispersion profiles measured along the position angle are shown as pink lines and the best-fit arctangent function fit to the rotation curve at the position angle are included as a gray solid line. The dependence of the measured velocity dispersion profiles on position angle is negligible and central velocity dispersions differ by ∼1% on average. The velocity profiles exhibit a stronger dependence on position angle, but the effect is small, comprising a median decrease in $|V_5|/\sigma_0$ of 8%. We emphasize that this does not account for any possible misalignment between the kinematic and photometric axes, which can be misaligned by as much as 50% (Emsellem et al. 2007). However, we note that this is not a dominant effect for this study, as the substantial effects of beam smearing due to the significant size of the PSF relative to the galaxy sizes in the LEGA-C sample dwarf the effects of up to 45° of misalignment in this exercise. The profiles are also shown after convolution and luminosity-weighted extraction within a 7.5 kpc wide slit as black (velocity) and red (velocity dispersion) dashed lines. A line in included in the lower left of each panel indicating the fixed physical scale of 5 kpc at which the velocity V_5 is measured.
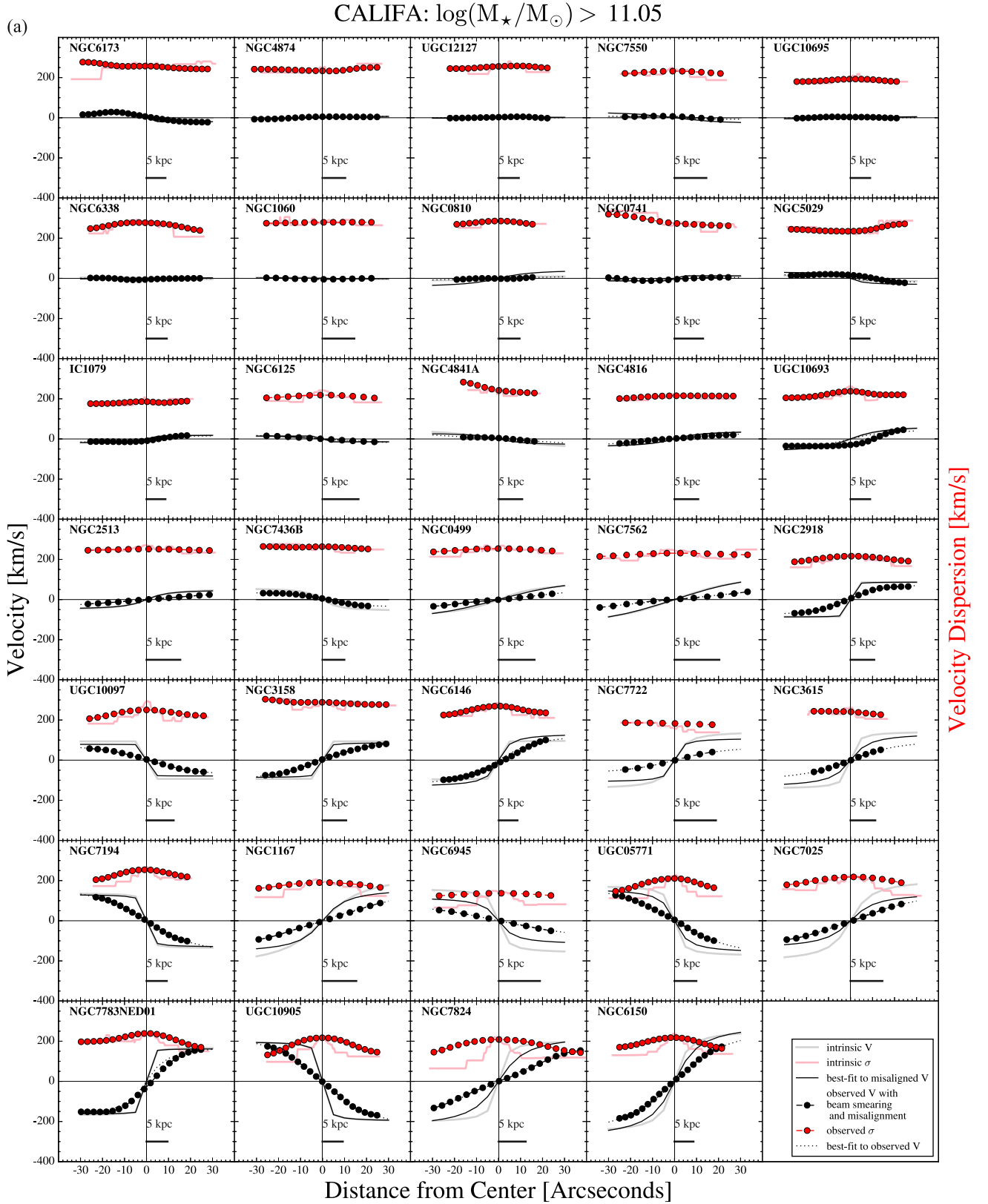
Figure 14. (a) Stellar rotation curves (black) and velocity dispersion profiles (red) for the highest-mass (log $M_*/M_\odot > 11.4$) sample of quiescent massive galaxies in the CALIFA stellar kinematics sample, ordered by ascending velocity. Rotational velocity is measured from best-fit arctangent functions at a radius of 5 kpc from the central pixel. Measured rotational velocities and velocity dispersions in Voronoi bins along the position angle are indicated by light gray and pink solid lines respectively, which we refer to as the intrinsic values. The best-fit arctangent rotation curve along the N–S or E–W simulated LEGA-C misaligned position angle is shown as solid black line. The measured velocity and velocity dispersions within LEGA-C sized "pixels" and including the effects of slit misalignment and beam smearing are shown by black and red symbols and the best-fit arctangent function to this simulated rotation curve is shown by the black dotted line. (b) Stellar rotation curves (black) and velocity dispersion profiles (red) for intermediate-mass quiescent massive galaxies in CALIFA, ordered by ascending velocity. (c) Stellar rotation curves (black) and velocity dispersion profiles (red) for the lowest-mass quiescent galaxies in CALIFA, ordered by ascending velocity.
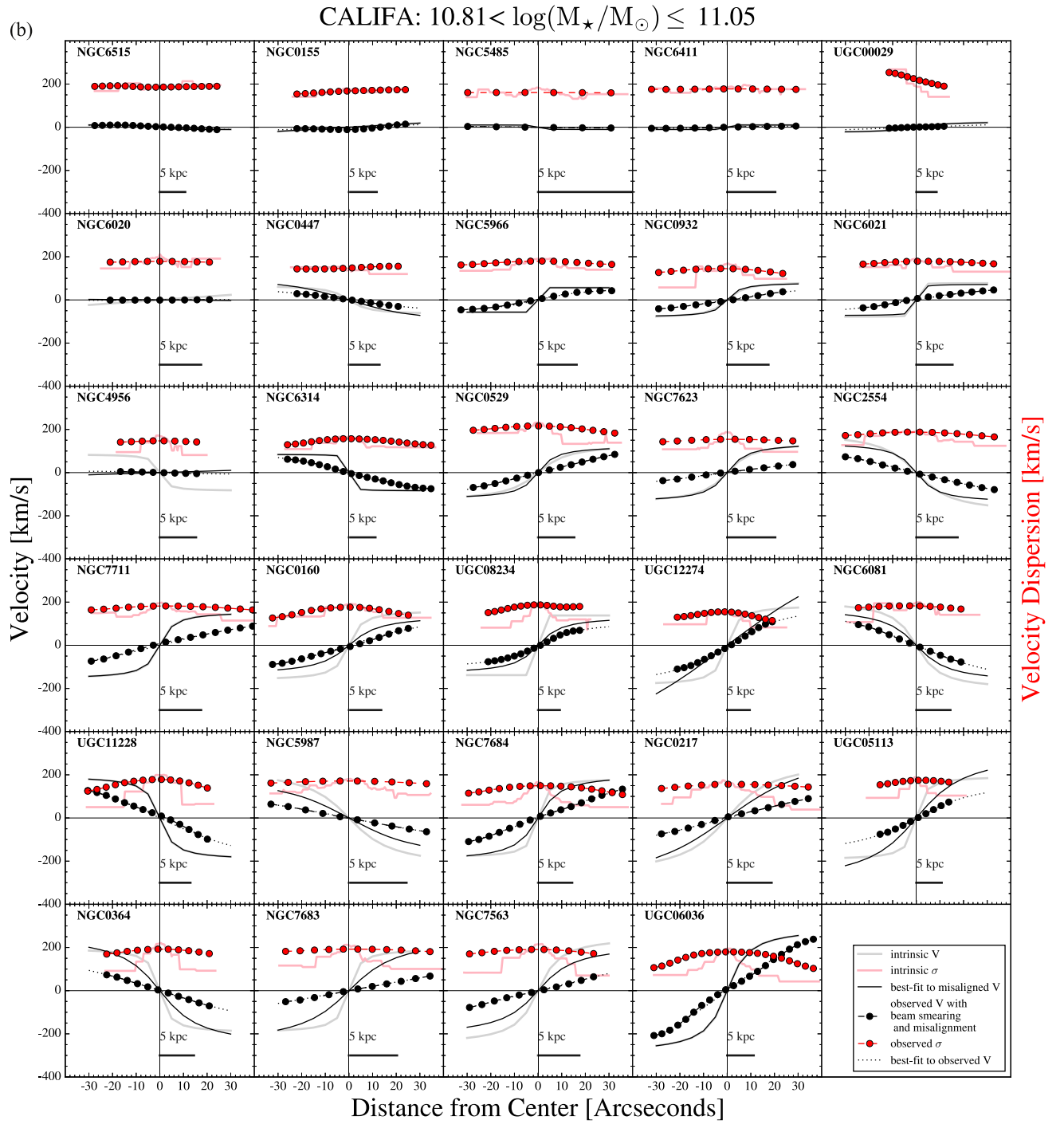
CALIFA: $10.81 < \log(M_\star/M_\odot) \leq 11.05$
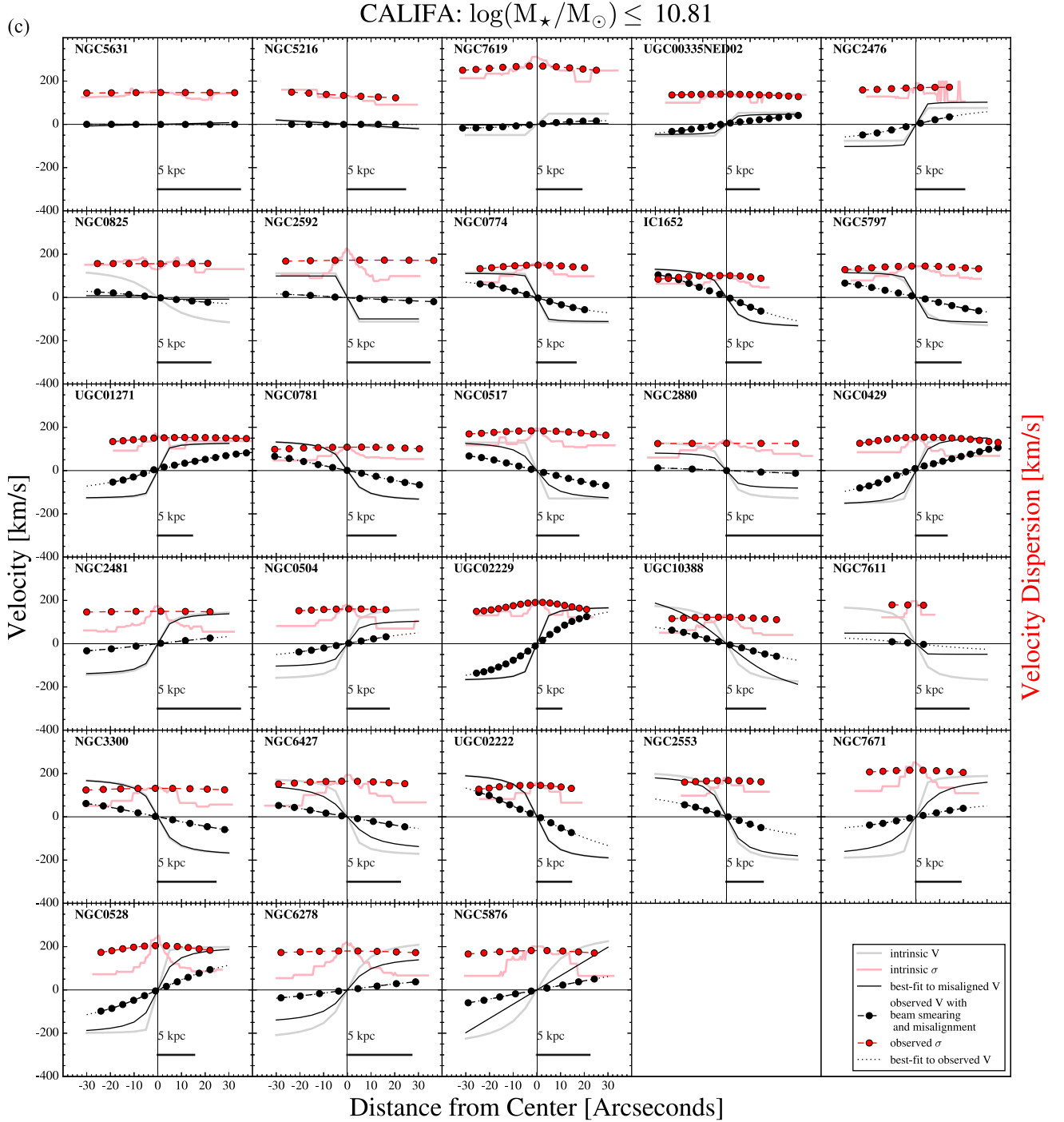

Figure 14. (Continued.)

Figure 14. (Continued.)

Appendix B
On the Choice of Velocity Aperture

In this paper, we adopt a measure of rotation within a fixed physical aperture, both for studying the properties of the LEGA-C sample and for comparison with the CALIFA data set. This has two primary advantages. First, measuring velocity within a fixed aperture of 5 kpc means that the bias on the measured rotational velocity introduced by beam smearing will

be roughly the same for all galaxies in the sample; the rotational velocity within an aperture that scales with the effective radius of a galaxy would be impacted differently for large and small galaxies. Second, we expect the sizes of massive galaxies to evolve through cosmic time (e.g., van der Wel et al. 2014b). We believe that that evolution is largely inside-out growth driven by minor-merging (e.g., Bezanson et al. 2009; Hopkins et al. 2009; van Dokkum et al. 2010), especially at $z \leqslant 1$ where this study is focused (Newman
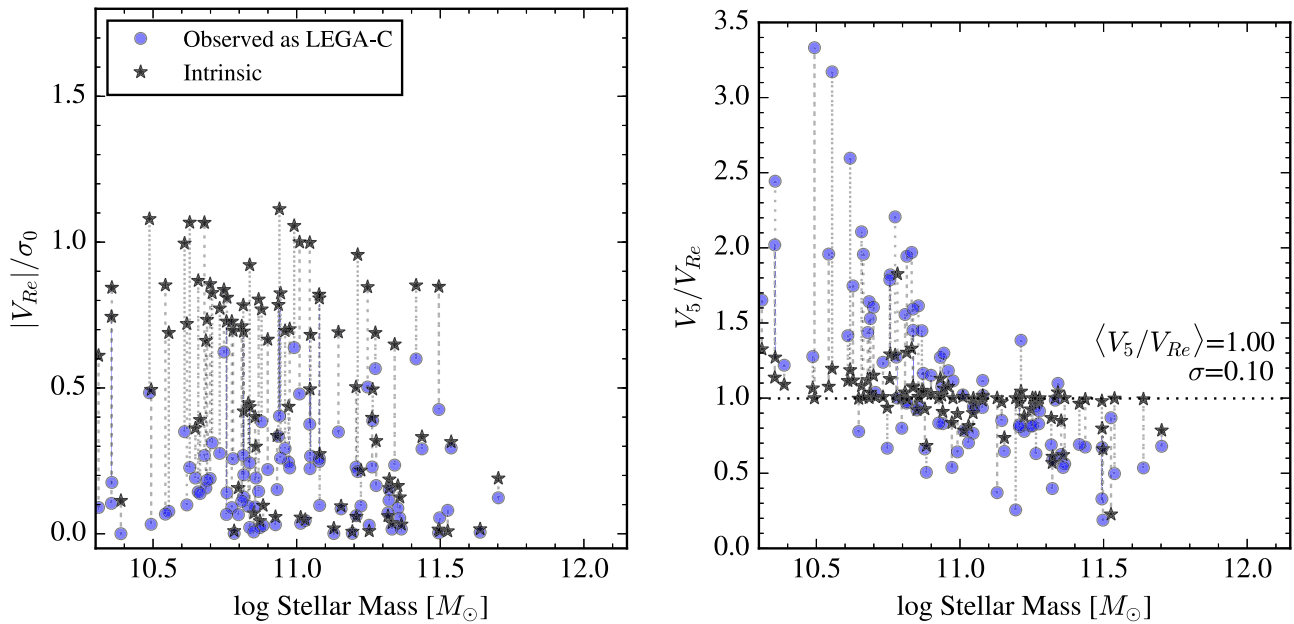
Figure 15. Measured velocity within an effective radius in CALIFA galaxies measured directly from the stellar kinematic maps (black) and from those blurred with the 3 kpc PSF (blue). As in Figure 10, this definition of reveals that the rotational support within the CALIFA data set is a strong function of stellar mass. However, unlike a velocity defined within a fixed aperture, the effect of beam smearing on the measured velocity within an effective radius is significantly stronger for less massive, and therefore more compact, galaxies.

et al. 2012). In this framework, we would expect galaxies to grow in size, and mass by building up a more diffuse envelope around a dense central core. By focusing on the rotational support within a *fixed* physical aperture, we probe the physical evolution of the same region of the galaxy, minimizing the additional confusion of whether the rotational support is physically evolving or whether it is the effect of using a redshift-evolving aperture.

However, in this appendix, we investigate the effects of defining the velocity at the effective radius (V_{Re}) of each galaxy. To demonstrate the impact of this, we begin by recreating the $|V|/\sigma$ versus stellar mass relation for the CALIFA galaxies in Figure 15 using the velocity calculated within an effective radius (V_{Re}). The left panel shows the measured $|V_{Re}|/\sigma$ before and after convolution, similar to Figure 10. Although the intrinsic points (black stars) show a very similar inverse correlation with stellar mass as with the velocity measured within 5 kpc, after convolving with a 3 kpc PSF the measured rotational support for low-mass galaxies, for which half-light radii are smaller than 5 kpc, is dramatically diminished. We expect the effect to be even stronger at $z \sim 0.8$, where LEGA-C galaxies are even more compact at fixed mass. The right panel of Figure 15 shows the ratio of the two velocity measures versus stellar mass from the intrinsic (black stars) and blurred kinematic maps (blue circles). The excellent agreement between the intrinsic V_5/V_{Re}, with an average ratio of 1.0 and a scatter of ∼0.1, suggests that either measure can be used to reliably assess the degree of projected rotation in the CALIFA data set. However, after PSF convolution, the two measures diverge dramatically, with a very clear effect as a function of stellar mass.

The second issue we wish to address in this appendix is our use of a fixed physical aperture and its impact on the measured evolution of rotational support. Figure 16 shows the size versus stellar mass (left panel) and velocity dispersion (right panel) relations for the LEGA-C and CALIFA samples. In this figure,

size corresponds to the semimajor axis of a best-fitting Sérsic model for the LEGA-C sample, and for CALIFA it is the half-light-major axis derived using growth curve analysis (Walcher et al. 2014). These two methodologies can yield biased size measurements; Méndez-Abreu et al. (2017) found significant offsets between single Sérsic fits and half-light major axis (HLMA) for CALIFA galaxies, which can differ by up to a factor of ∼2.5, a scatter of ∼20%, and a bias toward larger Sérsic effective radius than growth curve-derived HLMA. Therefore the relative evolution could be even stronger than suggested by this comparison. Furthermore, this measurement discrepancy is an additional factor in avoiding the use of a velocity aperture that scales with galaxy size. Given that we see clear evolution in galaxy sizes, we emphasize that only by measuring within a fixed physical aperture can we probe intrinsic evolution in the stellar orbits and rotational support. This necessarily implies that we are measuring the rotational support within a different fraction of galaxies at the two epochs. However, the combination of the observational effects inherent in our measurements and the observed size evolution between $z \sim 0$ and $z \sim 0.8$ leads us to conclude that measuring the velocity within a fixed physical aperture is the best course of action, settling on 5 kpc which roughly equals the extent of the least extended rotation curves in both surveys.

From Figure 16 it is clear that a 5 kpc aperture corresponds to a larger fraction of the LEGA-C galaxies than for those in the CALIFA sample. The average size of galaxies in the CALIFA sample is 1.5 times larger than in the LEGA-C sample. Given that many of the CALIFA rotation curves are still rising at 5 kpc, at least some fraction of the observed discrepancy in rotational support between the two samples could be driven by size evolution. To investigate this effect, we scale the velocity aperture for the CALIFA data set to 7.5 kpc and compare V/σ_0 at fixed velocity dispersion to those measured for the LEGA-C sample within 5 kpc. The results of this test are shown in Figure 17. The left panel of this figure shows $|V_{7.5}|/\sigma_0$ versus
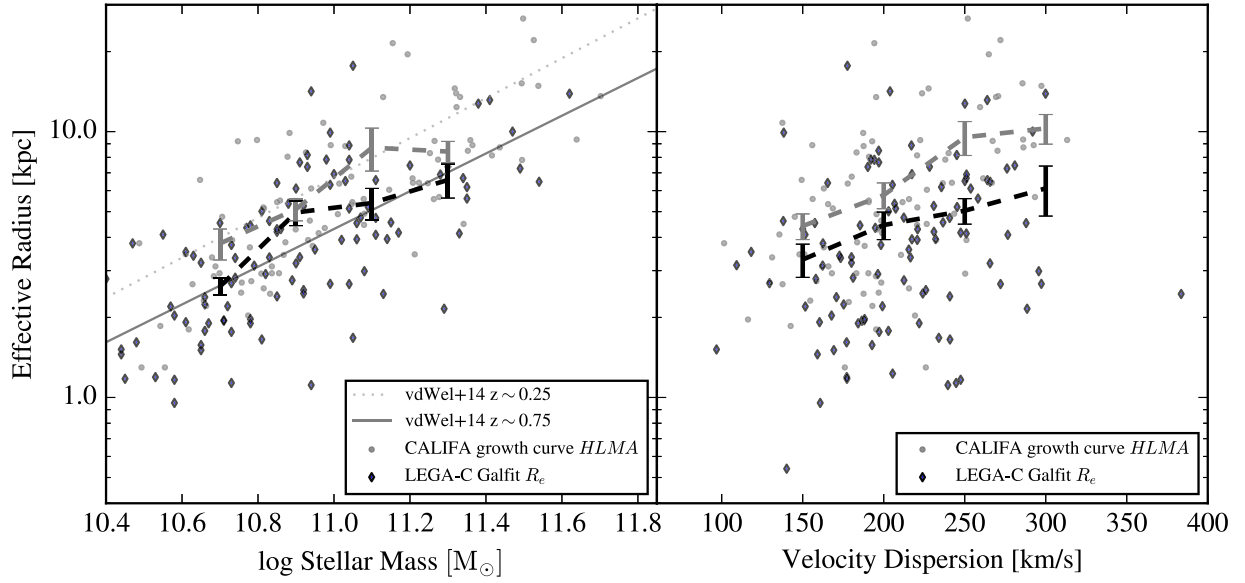
Figure 16. Size vs. stellar mass (left panel) and velocity dispersion (right panel) for CALIFA (half-light major axis radius, black) and LEGA-C (Sérsic half-light radius, gray) data sets. The running mean and scatter are indicated by dashed gray and black lines and the measured size-mass trends from van der Wel et al. (2014b) at $z \sim 0.25$ and $z \sim 0.75$ are indicated by dotted and solid lines respectively. At fixed mass and velocity dispersion CALIFA galaxies are more extended than those in the LEGA-C survey, confirming the expected trend of size evolution in the population of massive, quiescent galaxies.
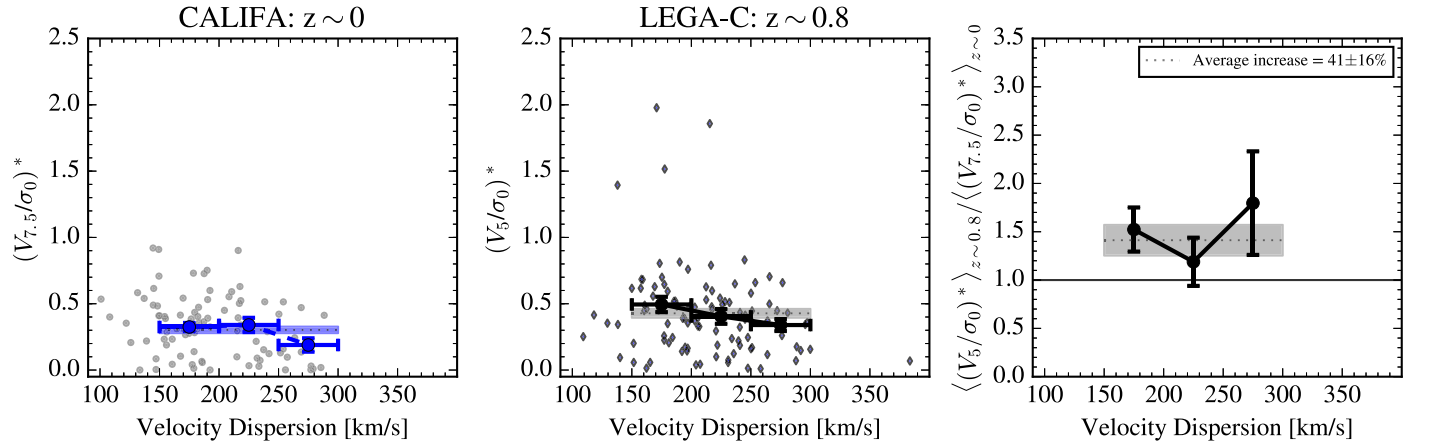

Figure 17. Rotational support $((V/\sigma_0)^*)$ vs. central velocity dispersion (σ_0) within an aperture that scales with increasing radius between the two samples. The left panel includes $|V_{7.5}|/\sigma_0$ for the simulated CALIFA $z \sim 0$ galaxies and the center panel includes LEGA-C galaxies at $z \sim 0.8$, for which velocities are measured within 5 kpc. The right panel shows the ratio of the averages in small running bins (indicated by black points with errorbars) and the overall (for $150 < \sigma/\mathrm{km\,s}^{-1} < 300$) given by the gray band. Even within an aperture that scales with average effective radius, $|V|/\sigma$ is higher by $41 \pm 16\%$ at $z \sim 0.8$.

velocity dispersion for CALIFA galaxies and the center panel shows $|V_5|/\sigma_0$ for LEGA-C galaxies. In each panel the running averages are indicated by solid blue and black lines with errorbars and the overall average and measurement uncertainty is included as a gray dotted line and horizontal band. All uncertainties in the averages are calculated via jackknife resampling. As expected from the rotation curves in Figure 14, the $|V|/\sigma_0$ values measured within a larger physical aperture are higher on average than within 5 kpc; however, the LEGA-C sample still exhibits slightly more rotational support. The right panel shows the ratio of the running and overall averages, indicating that, even when the velocity aperture is scaled to reflect the size evolution between the two epochs, we detect a $\sim 41 \pm 16\%$ decrease in the rotational support of quiescent galaxies since $z \sim 1$. This implied evolution is more subtle than what we measure within a fixed physical aperture, but is still statistically significant.

Finally, we investigate the use of the maximum measured velocity ($V_{\max}$), defined as the value of the best-fitting arctangent function at the maximum extent of the measured rotation, averaged between the north and south directions. In many cases, this might provide the best estimate of the intrinsic maximum rotational velocity. In Figure 18 we show the comparison between the rotational support measured at the maximum physical extent $((V_{\max}/\sigma_0)^*)$ versus velocity dispersion in the CALIFA and LEGA-C samples, as presented in Figures 13 and 17. The maximum measured rotational support for CALIFA galaxies is shown in the left panel and for the LEGA-C sample in the center panel. Following the symbols and plotting conventions in previous figures, solid symbols indicate individual galaxies, large symbols indicate the average values in three velocity bins, and the bands indicate the average $(V_{\max}/\sigma_0)^*$ between $150 < \sigma < 300$ in each sample. The right panel includes the ratio of the averages in three velocity
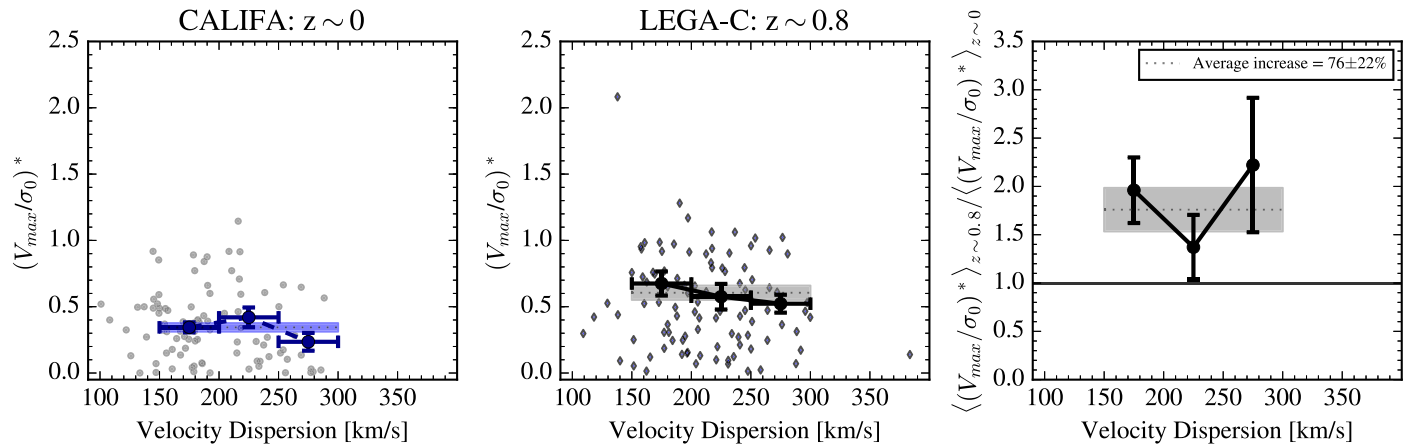
Figure 18. Rotational support at the maximum radial extent $((V_{max}/\sigma_0)^*)$ vs. central velocity dispersion (σ_0). The left panel includes $|V_{max}|/\sigma_0$ for the simulated CALIFA $z \sim 0$ galaxies and in the center panel for LEGA-C galaxies at $z \sim 0.8$. The right panel shows the ratio of the averages in small running bins (indicated by black points with errorbars) and the overall (for $150 < \sigma/\mathrm{km\,s^{-1}} < 300$) given by the gray band. Within this maximum radius, $|V|/\sigma$ is higher by $76 \pm 22\%$ at $z \sim 0.8$, which implies slightly less dramatic, but still significant, rotation than for velocities defined within 5 kpc.

dispersion bins (black error bars) and over the full range (gray band). The rotational support $((V_{max}/\sigma_0)^*)$ measured in this manner spans parameter space differently than defined at 5 kpc; values are higher on average at the maximum extent of the rotation curves than at 5 kpc. This is not surprising as most rotation curves in both samples do not flatten out (at LEGA-C seeing) and generally extend beyond 5 kpc. However, the qualitative comparison between the CALIFA and LEGA-C rotational support yields a similar result with this V_{max} definition as with V_5 (Figure 13): galaxies in the LEGA-C sample exhibit $76 \pm 22\%$ higher average rotational support, measured by $(V_{max}/\sigma_0)^*$, which is $\sim 1\sigma$ below the comparison at a fixed 5 kpc aperture. We note that this aperture is less consistent within an individual sample (e.g., as a function of stellar mass, effective radius, or Sérsic index) or between the two data sets, as the depths of the surveys are not perfectly matched. Therefore, although this may well come closer to the intrinsic values of V_{max} for each individual galaxy, we rely primarily upon the 5 kpc aperture for the comparison in the main text of the paper. The qualitatively similar behavior for velocities measured within a variety of apertures (5 kpc, evolving apertures to correct for galaxy size evolution, and at the maximum extend probed by the current data) supports our confidence in the implied evolution in rotational support of quiescent galaxies since $z \sim 1$.

ORCID iDs

Arjen van der Wel ● https://orcid.org/0000-0002-5027-0135
Camilla Pacifici ● https://orcid.org/0000-0003-4196-0617
Ivana Barišić ● https://orcid.org/0000-0001-6371-6274
Eric F. Bell ● https://orcid.org/0000-0002-5564-9873
Gabriel B. Brammer ● https://orcid.org/0000-0003-2680-005X
Priscilla Chauke ● https://orcid.org/0000-0002-1442-984X
Pieter van Dokkum ● https://orcid.org/0000-0002-8282-9888
Marijn Franx ● https://orcid.org/0000-0002-8871-3026
Anna Gallazzi ● https://orcid.org/0000-0002-9656-1800
Ivo Labbé ● https://orcid.org/0000-0002-2057-5376
Michael V. Maseda ● https://orcid.org/0000-0003-0695-4414
Adam Muzzin ● https://orcid.org/0000-0002-9330-9108
Jesse van de Sande ● https://orcid.org/0000-0003-2552-0021
David Sobral ● https://orcid.org/0000-0001-8823-4845

Caroline Straatman ● https://orcid.org/0000-0001-5937-4590
Po-Feng Wu ● https://orcid.org/0000-0002-9665-0440

References

Aihara, H., Armstrong, R., Bickerton, S., et al. 2018, PASJ, 70, S8
Astropy Collaboration, Robitaille, T. P., Tollerud, E. J., et al. 2013, A&A, 558, A33
Baldwin, J. A., Phillips, M. M., & Terlevich, R. 1981, PASP, 93, 5
Barden, M., Häußler, B., Peng, C. Y., McIntosh, D. H., & Guo, Y. 2012, MNRAS, 422, 449
Behroozi, P. S., Marchesini, D., Wechsler, R. H., et al. 2013, ApJL, 777, L10
Bell, E. F., Naab, T., McIntosh, D. H., et al. 2006, ApJ, 640, 241
Belli, S., Newman, A. B., & Ellis, R. S. 2014a, ApJ, 783, 117
Belli, S., Newman, A. B., & Ellis, R. S. 2017, ApJ, 834, 18
Belli, S., Newman, A. B., Ellis, R. S., & Konidaris, N. P. 2014b, ApJL, 788, L29
Bezanson, R., van Dokkum, P., & Franx, M. 2012, ApJ, 760, 62
Bezanson, R., van Dokkum, P. G., Tal, T., et al. 2009, ApJ, 697, 1290
Binney, J. 1978, MNRAS, 183, 501
Brammer, G. B., van Dokkum, P. G., & Coppi, P. 2008, ApJ, 686, 1503
Brinchmann, J., Charlot, S., White, S. D. M., et al. 2004, MNRAS, 351, 1151
Bruzual, G., & Charlot, S. 2003, MNRAS, 344, 1000
Calzetti, D., Armus, L., Bohlin, R. C., et al. 2000, ApJ, 533, 682
Cano-Díaz, M., Sánchez, S. F., Zibetti, S., et al. 2016, ApJL, 821, L26
Cappellari, M. 2016, ARA&A, 54, 597
Cappellari, M. 2017, MNRAS, 466, 798
Cappellari, M., & Emsellem, E. 2004, PASP, 116, 138
Cappellari, M., Emsellem, E., Bacon, R., et al. 2007, MNRAS, 379, 418
Carollo, C. M., Bschorr, T. J., Renzini, A., et al. 2013, ApJ, 773, 112
Chabrier, G. 2003, PASP, 115, 763
Chang, Y.-Y., van der Wel, A., Rix, H.-W., et al. 2013, ApJ, 773, 149
Chevance, M., Weijmans, A.-M., Damjanov, I., et al. 2012, ApJL, 754, L24
Cortese, L., Fogarty, L. M. R., Bekki, K., et al. 2016, MNRAS, 463, 170
Daddi, E., Renzini, A., Pirzkal, N., et al. 2005, ApJ, 626, 680
Davies, R. L., Efstathiou, G., Fall, S. M., Illingworth, G., & Schechter, P. L. 1983, ApJ, 266, 41
Emsellem, E., Cappellari, M., Krajnović, D., et al. 2007, MNRAS, 379, 401
Emsellem, E., Cappellari, M., Krajnović, D., et al. 2011, MNRAS, 414, 888
Faber, S. M., & Jackson, R. E. 1976, ApJ, 204, 668
Fagioli, M., Carollo, C. M., Renzini, A., et al. 2016, ApJ, 831, 173
Falcón-Barroso, J., Lyubenova, M., van de Ven, G., et al. 2017, A&A, 597, A48
Fogarty, L. M. R., Scott, N., Owers, M. S., et al. 2014, MNRAS, 443, 485
Fogarty, L. M. R., Scott, N., Owers, M. S., et al. 2015, MNRAS, 454, 2050
Förster Schreiber, N. M., Genzel, R., Bouché, N., et al. 2009, ApJ, 706, 1364
Förster Schreiber, N. M., Shapley, A. E., Erb, D. K., et al. 2011, ApJ, 731, 65
Franx, M., Illingworth, G., & Heckman, T. 1989, AJ, 98, 538
Franx, M., & van Dokkum, P. G. 1996, in IAU Symp. 171, New Light on Galaxy Evolution, ed. R. Bender & R. L. Davies (Dordrecht: Kluwer), 233
Genel, S., Fall, S. M., Hernquist, L., et al. 2015, ApJL, 804, L40

Girardi, L., Bressan, A., Bertelli, G., & Chiosi, C. 2000, A&AS, 141, 371
Glazebrook, K., Schreiber, C., Labbé, I., et al. 2017, Natur, 544, 71
Graham, M. T., Cappellari, M., Li, H., et al. 2018, MNRAS, arXiv:1802.08213
Harrison, C. M., Johnson, H. L., Swinbank, A. M., et al. 2017, MNRAS, 467, 1965
Hilz, M., Naab, T., & Ostriker, J. P. 2013, MNRAS, 429, 2924
Hopkins, P. F., Bundy, K., Murray, N., et al. 2009, MNRAS, 398, 898
Hopkins, P. F., Cox, T. J., Kereš, D., & Hernquist, L. 2008, ApJS, 175, 390
Johnston, E. J., Merrifield, M. R., Aragón-Salamanca, A., & Cappellari, M. 2013, MNRAS, 428, 1296
Kassin, S. A., Weiner, B. J., Faber, S. M., et al. 2007, ApJL, 660, L35
Kewley, L. J., Dopita, M. A., Sutherland, R. S., Heisler, C. A., & Trevena, J. 2001, ApJ, 556, 121
Khochfar, S., Emsellem, E., Serra, P., et al. 2011, MNRAS, 417, 845
Koekemoer, A. M., Aussel, H., Calzetti, D., et al. 2007, ApJS, 172, 196
Kormendy, J. 1982, in Proc. Twelfth Advanced Course, Morphology and Dynamics of Galaxies (Sauverny: Observatoire de Geneve), 113
Krajnović, D., Emsellem, E., Cappellari, M., et al. 2011, MNRAS, 414, 2923
Kriek, M., van Dokkum, P. G., Franx, M., et al. 2008, ApJ, 677, 219
Kriek, M., van Dokkum, P. G., Labbé, I., et al. 2009, ApJ, 700, 221
Leja, J., van Dokkum, P., & Franx, M. 2013, ApJ, 766, 33
Lilly, S. J., & Carollo, C. M. 2016, ApJ, 833, 1
Lotz, J. M., Jonsson, P., Cox, T. J., et al. 2011, ApJ, 742, 103
Man, A. W. S., Zirm, A. W., & Toft, S. 2016, ApJ, 830, 89
Martig, M., Bournaud, F., Teyssier, R., & Dekel, A. 2009, ApJ, 707, 250
Massey, R., Stoughton, C., Leauthaud, A., et al. 2010, MNRAS, 401, 371
McCracken, H. J., Milvang-Jensen, B., Dunlop, J., et al. 2012, A&A, 544, A156
McDermid, R. M., Alatalo, K., Blitz, L., et al. 2015, MNRAS, 448, 3484
Méndez-Abreu, J., Ruiz-Lara, T., Sánchez-Menguiano, L., et al. 2017, A&A, 598, A32
Moran, S. M., Loh, B. L., Ellis, R. S., et al. 2007, ApJ, 665, 1067
Muzzin, A., Marchesini, D., Stefanon, M., et al. 2013a, ApJS, 206, 8
Muzzin, A., Marchesini, D., Stefanon, M., et al. 2013b, ApJ, 777, 18
Muzzin, A., Marchesini, D., van Dokkum, P. G., et al. 2009, ApJ, 701, 1839
Naab, T., Johansson, P. H., & Ostriker, J. P. 2009, ApJL, 699, L178
Naab, T., Oser, L., Emsellem, E., et al. 2014, MNRAS, 444, 3357
Newman, A. B., Belli, S., & Ellis, R. S. 2015, ApJL, 813, L7
Newman, A. B., Ellis, R. S., Bundy, K., & Treu, T. 2012, ApJ, 746, 162
Oser, L., Naab, T., Ostriker, J. P., & Johansson, P. H. 2011, ApJ, 744, 63
Patel, S. G., van Dokkum, P. G., Franx, M., et al. 2013, ApJ, 766, 15
Peng, C. Y., Ho, L. C., Impey, C. D., & Rix, H.-W. 2002, AJ, 124, 266
Poggianti, B. M., Calvi, R., Bindoni, D., et al. 2013, ApJ, 762, 77
Price, S. H., Kriek, M., Shapley, A. E., et al. 2016, ApJ, 819, 80
Robaina, A. R., Bell, E. F., van der Wel, A., et al. 2010, ApJ, 719, 844
Sánchez, S. F., García-Benito, R., Zibetti, S., et al. 2016, A&A, 594, A36
Sánchez, S. F., Kennicutt, R. C., Gil de Paz, A., et al. 2012, A&A, 538, A8
Sánchez-Blázquez, P., Peletier, R. F., Jiménez-Vicente, J., et al. 2006, MNRAS, 371, 703
Simons, R. C., Kassin, S. A., Trump, J. R., et al. 2016, ApJ, 830, 14
Simons, R. C., Kassin, S. A., Weiner, B. J., et al. 2015, MNRAS, 452, 986

Simons, R. C., Kassin, S. A., Weiner, B. J., et al. 2017, ApJ, 843, 46
Straatman, C. M. S., Glazebrook, K., Kacprzak, G. G., et al. 2017, ApJ, 839, 57
Tacconi, L. J., Neri, R., Genzel, R., et al. 2013, ApJ, 768, 74
Taylor, E. N., Franx, M., Glazebrook, K., et al. 2010, ApJ, 720, 723
Toft, S., van Dokkum, P., Franx, M., et al. 2007, ApJ, 671, 285
Toft, S., Zabl, J., Richard, J., et al. 2017, Natur, 546, 510
Torrey, P., Wellons, S., Ma, C.-P., Hopkins, P. F., & Vogelsberger, M. 2017, MNRAS, 467, 4872
Torrey, P., Wellons, S., Machado, F., et al. 2015, MNRAS, 454, 2770
Trujillo, I., Aguerri, J. A. L., Cepa, J., & Gutiérrez, C. M. 2001, MNRAS, 328, 977
Trujillo, I., Cenarro, A. J., de Lorenzo-Cáceres, A., et al. 2009, ApJL, 692, L118
Trujillo, I., Conselice, C. J., Bundy, K., et al. 2007, MNRAS, 382, 109
Valentinuzzi, T., Fritz, J., Poggianti, B. M., et al. 2010a, ApJ, 712, 226
Valentinuzzi, T., Poggianti, B. M., Saglia, R. P., et al. 2010b, ApJL, 721, L19
van de Sande, J., Bland-Hawthorn, J., Fogarty, L. M. R., et al. 2017, ApJ, 835, 104
van de Sande, J., Kriek, M., Franx, M., et al. 2013, ApJ, 771, 85
van der Marel, R. P., & van Dokkum, P. G. 2007, ApJ, 668, 756
van der Wel, A., Bell, E. F., Häussler, B., et al. 2012, ApJS, 203, 24
van der Wel, A., Chang, Y.-Y., Bell, E. F., et al. 2014a, ApJL, 792, L6
van der Wel, A., Franx, M., van Dokkum, P. G., et al. 2014b, ApJ, 788, 28
van der Wel, A., Holden, B. P., Zirm, A. W., et al. 2008, ApJ, 688, 48
van der Wel, A., Noeske, K., Bezanson, R., et al. 2016, ApJS, 223, 29
van der Wel, A., Rix, H.-W., Holden, B. P., Bell, E. F., & Robaina, A. R. 2009, ApJL, 706, L120
van der Wel, A., Rix, H.-W., Wuyts, S., et al. 2011, ApJ, 730, 38
van der Wel, A., & van der Marel, R. P. 2008, ApJ, 684, 260
van Dokkum, P. G., Franx, M., Fabricant, D., Illingworth, G. D., & Kelson, D. D. 2000, ApJ, 541, 95
van Dokkum, P. G., Franx, M., Kriek, M., et al. 2008, ApJL, 677, L5
van Dokkum, P. G., Leja, J., Nelson, E. J., et al. 2013, ApJL, 771, L35
van Dokkum, P. G., Nelson, E. J., Franx, M., et al. 2015, ApJ, 813, 23
van Dokkum, P. G., Whitaker, K. E., Brammer, G., et al. 2010, ApJ, 709, 1018
Vazdekis, A. 1999, ApJ, 513, 224
Veale, M., Ma, C.-P., Thomas, J., et al. 2017, MNRAS, 464, 356
Vogt, N. P., Forbes, D. A., Phillips, A. C., et al. 1996, ApJL, 465, L15
Vogt, N. P., Phillips, A. C., Faber, S. M., et al. 1997, ApJL, 479, L121
Walcher, C. J., Wisotzki, L., Bekeraité, S., et al. 2014, A&A, 569, A1
Weiner, B. J., Willmer, C. N. A., Faber, S. M., et al. 2006, ApJ, 653, 1049
Whitaker, K. E., Kriek, M., van Dokkum, P. G., et al. 2012a, ApJ, 745, 179
Whitaker, K. E., van Dokkum, P. G., Brammer, G., & Franx, M. 2012b, ApJL, 754, L29
Williams, C. C., Giavalisco, M., Bezanson, R., et al. 2016, arXiv:1607.06089
Wisnioski, E., Förster Schreiber, N. M., Wuyts, S., et al. 2015, ApJ, 799, 209
Wuyts, S., Cox, T. J., Hayward, C. C., et al. 2010, ApJ, 722, 1666
Wuyts, S., Förster Schreiber, N. M., Wisnioski, E., et al. 2016, ApJ, 831, 149
Yano, M., Kriek, M., van der Wel, A., & Whitaker, K. E. 2016, ApJL, 817, L21